Review

A Brief Review of Atomistic Studies on the $BaTiO_3$ Photocatalyst for Solar Water Splitting

Aisulu U. Abuova , Ulzhan Zh. Tolegen , Talgat M Inerbaev , Mirat Karibayev , Balzhan M.Satanova , Fatima U Abuova * , Anatoli I Popov *

Posted Date: 6 June 2025

doi: 10.20944/preprints202506.0553.v1

Keywords: BaTiO3; doping; defect engineering; surface functionalization; atomistic study; photocatalytic water splitting

 doi:10.20944/preprints202506.0553.v1

Review

A Brief Review of Atomistic Studies on the $BaTiO_3$ Photocatalyst for Solar Water Splitting

Aisulu U. Abuova [1], Ulzhan Zh. Tolegen [1], Talgat M. Inerbaev [1,2], Mirat Karibayev [3], Balzhan M.Satanova [1], Fatima U. Abuova [1,*] and Anatoli I. Popov [1,4,*]

[1] Institute of Physical and Technical Sciences, L. N. Gumilyov Eurasian National University, 010000, Astana, Kazakhstan

[2] Vernadsky Institute of Geochemistry and Analytical Chemistry, Russian Academy of Science, 119991 Moscow, Russia

[3] Laboratory of Renewable Energy, National Laboratory Astana, Nazarbayev University, 010000, Astana;

[4] Institute of Solid State Physics, University of Latvia, Kengaraga 8, LV-1063 Riga, Latvia

* Correspondence: abuova_fu@enu.kz (F.U.A.); popov@latnet.lv (A.I.P.)

Abstract: $BaTiO_3$ has emerged as a promising photocatalyst for solar-driven water splitting due to its unique ferroelectric, piezoelectric, and electronic properties. This review provides a comprehensive analysis of atomistic simulation studies on $BaTiO_3$, highlighting the role of Density Functional Theory (DFT), ab initio Molecular Dynamics (MD), and classical all-atom MD in exploring its photocatalytic behavior. DFT studies have offered valuable insights into the electronic structure, density of state, optical properties, band gap engineering and others of $BaTiO_3$, while MD simulations have enabled a dynamic understanding of water-splitting mechanisms at finite temperatures. The review discusses the impact of doping, surface modifications, and defect engineering on enhancing charge separation and reaction kinetics. Key findings from recent computational works are summarized, offering a deeper understanding of $BaTiO_3$'s photocatalytic activity. This study underscores the significance of advanced multi scale simulation techniques in optimizing $BaTiO_3$ for solar water splitting and provides perspectives for future research in developing high-performance photocatalytic materials.

Keywords: $BaTiO_3$; doping; defect engineering; surface functionalization; atomistic study; photocatalytic water splitting

1. Introduction

Green hydrogen is a promising alternative fuel produced from renewable energy sources, playing a crucial role in achieving a carbon-free energy landscape. Unlike conventional hydrogen production methods that rely on fossil fuels, green hydrogen is generated through environmentally friendly techniques, reducing carbon emissions and supporting sustainable energy transitions in line with the Paris Agreement [1–3]. Several key methods are employed to produce green hydrogen efficiently. Several key methods are employed to produce green hydrogen efficiently, including (i) steam methane reforming (SMR) with carbon capture, (ii) electrolysis, (iii) biomass gasification, (iv) biological hydrogen production, (v) the hybrid Cu–Cl cycle, and (vi) solar-driven hydrogen production, all of which will be briefly discussed in the next paragraph.

Firstly, traditional SMR, which involves heating methane from natural gas with steam to produce hydrogen, carbon monoxide, and carbon dioxide, is not inherently a green process. However, when combined with carbon capture and storage technologies, it becomes "blue hydrogen," a lower-carbon alternative to traditional hydrogen production [4–6]. Although not fully green, this method serves as a transitional approach to reducing emissions.

Secondly, electrolysis is one of the most widely studied methods for green hydrogen production. This process splits water into oxygen and hydrogen using an electric current. When powered by renewable energy sources such as wind or solar power, the process is entirely carbon-free, classifying

 doi:10.20944/preprints202506.0553.v1

it as green hydrogen. Electrolysis is particularly suitable for applications requiring high-purity hydrogen and benefits from the increasing integration of renewable electricity into the global energy grid [7,8].

Thirdly, biomass gasification involves converting organic materials into hydrogen-rich syngas through high-temperature reactions. Since the carbon emissions from biomass are biogenic and do not contribute to additional atmospheric CO_2, this method presents a sustainable alternative to traditional fossil fuel-based hydrogen production [9,10].

Fourthly, microbial activity offers another sustainable hydrogen production method. Certain bacteria and microalgae can generate hydrogen by breaking down organic matter such as biomass or wastewater. This process not only produces hydrogen but also helps in waste management and organic matter recycling [11,12].

Fifthly, hybrid Cu-Cl cycle is an advanced thermochemical cycle that integrates nuclear heat, renewable energy, or industrial waste heat to produce hydrogen efficiently. Its potential scalability makes it an attractive option for large-scale hydrogen generation [13,14].

Lastly, several innovative solar-driven methods have been developed to harness sunlight for hydrogen generation. Photobiological processes utilize certain bacteria and green algae that produce hydrogen through photosynthesis, providing a bio-inspired and sustainable approach. Photoelectrochemical water splitting employs specialized semiconductors that absorb sunlight to drive water-splitting reactions, directly converting solar energy into hydrogen. Solar thermochemical hydrogen production leverages concentrated solar power to initiate chemical reactions, often involving metal oxides, to efficiently split water into hydrogen and oxygen. These solar-driven technologies offer environmentally friendly solutions for hydrogen production, contributing to the transition toward sustainable energy systems. Additionally, photocatalytic water splitting is another emerging technique that utilizes photocatalysts typically semiconductor materials such as TiO_2 or other metal oxides—to absorb sunlight and facilitate water decomposition into hydrogen and oxygen [15,16]. These photocatalysts enhance reaction efficiency by reducing activation energy and improving charge separation, making them a cost-effective and scalable option for hydrogen production.

1.1. Photocatalytic Water Splitting and Its Challenges

Figure 1 presents a schematic illustration of three distinct water-splitting methods: electrochemical, photoelectrochemical, and photocatalytic water splitting [17].

In electrochemical water splitting, an external electrical source drives the water electrolysis process, typically using alkaline or proton exchange membrane electrolyzers. Photo electrochemical water splitting combines light absorption and electrochemical reactions in a single system, where a semiconductor photoelectrode absorbs solar energy to generate charge carriers for water splitting. In photocatalytic water splitting, a photocatalyst directly absorbs sunlight to excite electrons, facilitating overall water splitting without external bias, though its efficiency remains lower than the other methods [18–22]. Photocatalytic water splitting relies on semiconductor photocatalysts that absorb light and generate electron-hole pairs, which facilitate redox reactions necessary for water decomposition.

 doi:10.20944/preprints202506.0553.v1

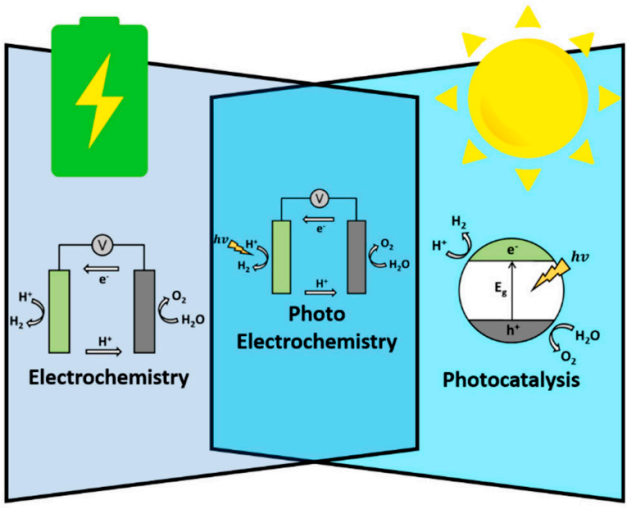

Figure 1. Schemes illustrate three major various water splitting methods [17].Reprinted with permission from [17]. Copyright 2020, for MDPI.

Various photocatalysts have been explored for their efficiency and stability in hydrogen production, including TiO_2, ZnO, CdS, WO_3, g-C_3N_4, and $BiVO_4$ [23–26]. Among these materials, perovskite-based photocatalysts have gained significant attention due to their excellent light absorption, charge separation efficiency, and structural tunability.

Despite its potential, photocatalytic water splitting faces several challenges that limit its efficiency and large-scale application including (i) low efficiency – many photocatalytic materials exhibit low solar-to-hydrogen conversion efficiencies, requiring further improvements to enhance practical viability; (ii) limited light absorption – some photocatalysts, such as TiO_2, primarily absorb ultraviolet light, which constitutes only a small fraction of the solar spectrum. This limits their overall efficiency in utilizing sunlight for hydrogen production; (iii) charge recombination – the photogenerated electron-hole pairs often recombine before participating in the water-splitting reaction, significantly reducing the quantum yield and overall hydrogen generation rate; (iv) photocorrosion – certain semiconductor materials, such as CdS, suffer from instability in aqueous solutions, undergoing degradation due to photocorrosion, which compromises their long-term performance; (v) high overpotentials – the water-splitting reaction requires overcoming high overpotentials, which slows down reaction kinetics and demands the use of additional co-catalysts to improve efficiency [26–30].

Addressing these challenges requires material modifications, such as doping, heterojunction formation, and surface engineering, to improve light absorption, charge separation, and stability. In this regard, $BaTiO_3$ has emerged as a promising photocatalyst for water splitting due to its strong ferroelectric properties, high chemical stability, and ability to enhance charge separation, thereby improving photocatalytic efficiency. This review focuses on the role of $BaTiO_3$ in photocatalytic water splitting. $BaTiO_3$, with its inherent ferroelectric properties and chemical stability, has shown promise in overcoming some of these limitations, making it a compelling candidate for photocatalytic water splitting applications.

1.2. Background of $BaTiO_3$for Photocatalytic Water Splitting

$BaTiO_3$ is an inorganic compound with a perovskite crystal structure, widely studied for its unique ferroelectric, piezoelectric, and dielectric properties. It is a wide-bandgap semiconductor that exhibits excellent chemical stability and high charge separation efficiency [31–33]. These characteristics make it highly valuable in various technological applications, including capacitors, sensors, microwave devices, and photocatalytic water splitting.

 doi:10.20944/preprints202506.0553.v1

The use of $BaTiO_3$ in microwave devices dates back to the early 1950s. Research found that adding Sr could decrease the Curie temperature, the transition point between its ferroelectric and paraelectric states, from approximately 120°C to room temperature. This led to the development of $Ba_{1-x}Sr_xTiO_3$, which gained significant interest due to its high dielectric constant, low dielectric loss, and high dielectric breakdown. Additionally, the composition-dependent Curie temperature of $Ba_{1-x}Sr_xTiO_3$ made it an attractive material for tunable microwave applications, including phase shifters and frequency-agile components in communication systems [34–36].

The chemical formula of barium titanate is $BaTiO_3$, and it is classified as the barium salt of metatitanic acid. It exhibits strong ferroelectric, piezoelectric, and pyroelectric properties, which contribute to its broad applicability. $BaTiO_3$ is a solid material with a high dielectric constant, making it useful in applications where charge storage and energy conversion are critical [35–38]. Its crystal structure undergoes several phase transitions depending on temperature, influencing its electrical and mechanical properties.

$BaTiO_3$ exhibits several polymorphs depending on temperature (Figure 2) [39]. At above ~120°C, it adopts a cubic ($Pm\bar{3}m$) perovskite structure, which is a paraelectric and centrosymmetric phase. Between ~5°C and 120°C, $BaTiO_3$ transitions to a tetragonal (P4mm) phase, a ferroelectric structure characterized by spontaneous polarization along the c-axis. As the temperature decreases further to between ~−90°C and 5°C, it takes on an orthorhombic (Amm2) phase, where the polarization shifts to a different direction compared to the tetragonal phase. Below ~−90°C, the material stabilizes in a rhombohedral (R3m) phase, with spontaneous polarization along the [111] direction. Additionally, $BaTiO_3$ can exist in a hexagonal (P63/mmc) phase under high-pressure or non-equilibrium conditions, but this phase is not a stable ferroelectric structure under normal conditions [39–42].

 doi:10.20944/preprints202506.0553.v1

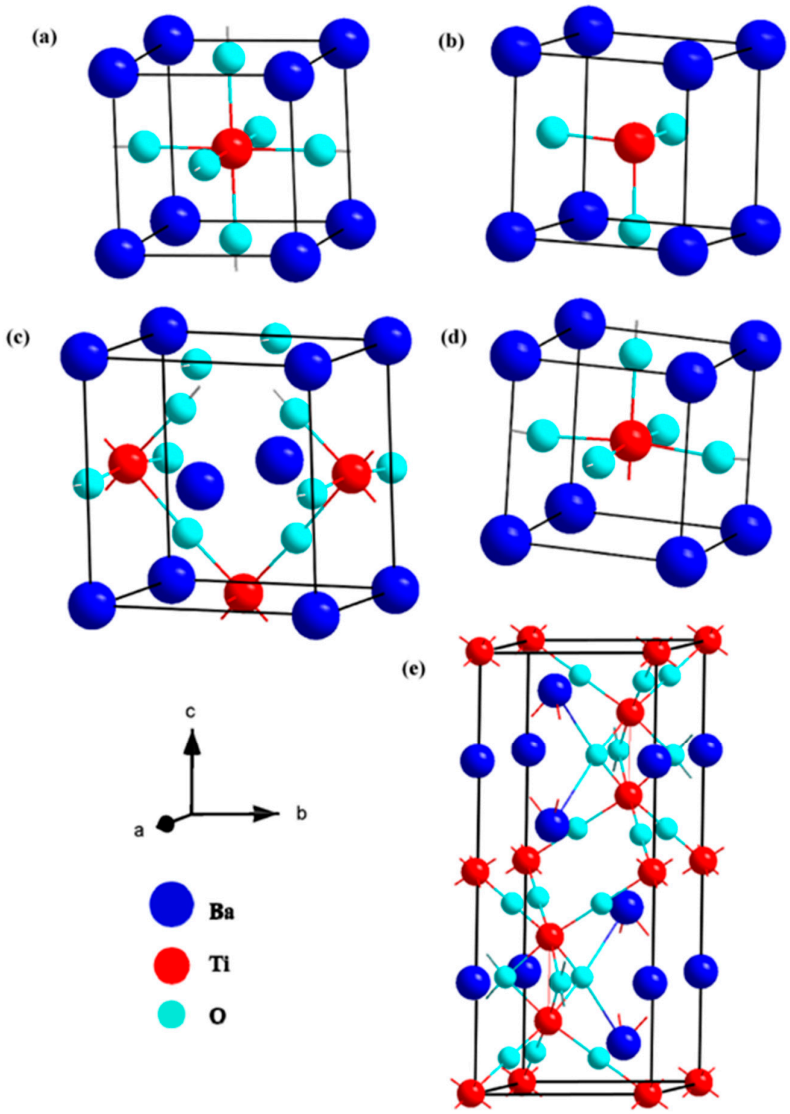

Figure 2. Atomistic representation of the $BaTiO_3$ polymorphs structures in different phases: (a) cubic, (b) rhombohedral, (c) orthorhombic, (d) tetragonal, and (e) hexagonal [39].Reprinted with permission from [39]. Copyright 2023, for Elsevier.

$BaTiO_3$ has widespread use in electronic and energy-related technologies. Its high dielectric constant makes it an essential component in capacitors, improving energy storage efficiency in consumer and industrial electronics. In sensor applications, its piezoelectric properties allow precise detection of mechanical and thermal changes, which is crucial in automotive and biomedical fields [41–45]. Additionally, $BaTiO_3$, along with $SrTiO_3$, plays a significant role in microwave tunable devices, contributing to the advancement of wireless communication technologies.

In the field of memory storage, $BaTiO_3$ is a promising candidate for replacing SiO_2 as a charge storage dielectric in dynamic random-access memory. Its superior charge retention capabilities could lead to more energy-efficient and higher-capacity memory devices [45–47]. Moreover, its integration into micro-electromechanical systems technology enables its use in micro-electromechanical systems switches, which are key components in modern phase shifters and adaptive electronic circuits.

$BaTiO_3$ is also widely researched for its potential in energy harvesting applications. As a ferroelectric and piezoelectric material, it can convert mechanical vibrations into electrical energy, making it useful in self-powered sensors and wearable electronics [48–50]. Additionally, $BaTiO_3$-

 doi:10.20944/preprints202506.0553.v1

based materials have been explored for their role in positive temperature coefficient resistors, where their resistivity increases with temperature, providing applications in thermal sensing and circuit protection.

One of the most promising applications of $BaTiO_3$ is in photocatalytic water splitting for hydrogen production. Due to its high charge separation efficiency and chemical stability, $BaTiO_3$ can act as an efficient photocatalyst, harnessing solar energy to drive the splitting of water into hydrogen and oxygen [50–55]. This process represents a sustainable method for hydrogen generation, contributing to the global shift toward renewable energy sources.

With its wide-ranging applications, $BaTiO_3$ continues to be an important material in modern technology. Its unique combination of electrical, dielectric, and structural properties enables innovations in energy storage, electronic devices, and environmental sustainability.

1.3. Application of Atomistic Study of $BaTiO_3$ Photocatalyst

Atomistic simulations play a crucial role in understanding the photocatalytic properties of $BaTiO_3$, providing insights at multiple scales through Density Functional Theory (DFT), ab initio Molecular Dynamics (MD), and classical all-atom MD simulations (Figure 3) [56].

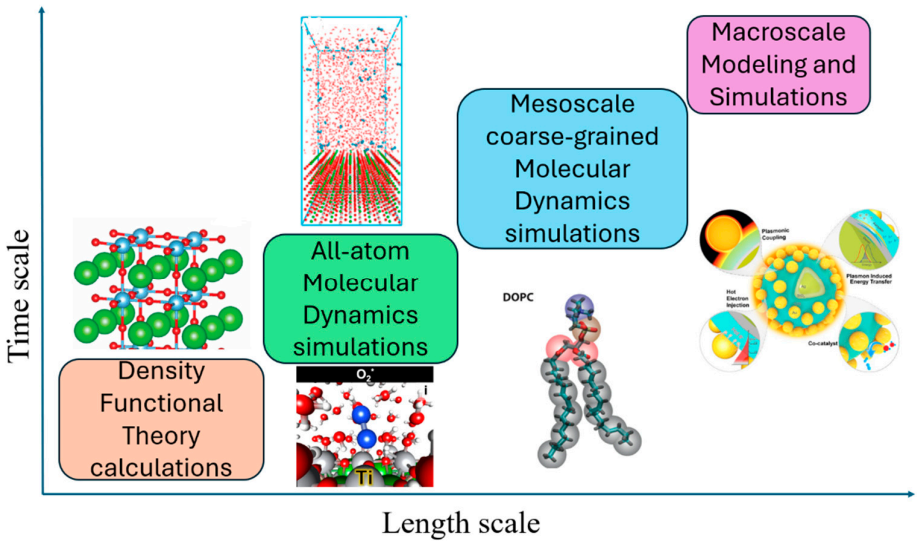

Figure 3. Illustration of different scales in computational engineering and material design. Reprinted with permission from [57–61]. Copyright 2024, for MDPI [57], copyright 2022, for the Elsevier [58], copyright 2024, for the arXiv [59], copyright 2013, for the MDPI [60], copyright 2020, for the American Chemical Society [61].

DFT is widely utilized to accurately describe the electronic structure, phase stability, and defect behavior of $BaTiO_3$ at the atomic level. It offers a cost-effective approach for investigating its ferroelectric and piezoelectric properties, which are crucial for photocatalytic activity. Given that $BaTiO_3$ undergoes multiple temperature-dependent phase transitions, DFT calculations help predict the relative stability of different polymorphs (cubic, tetragonal, orthorhombic, and rhombohedral) and their corresponding electronic and vibrational characteristics [63–65]. Moreover, DFT enables researchers to explore how external factors such as doping, strain, and electric fields modify the dielectric and electronic properties, making it invaluable for designing optimized photocatalytic materials.

Beyond structural analysis, DFT provides detailed insights into $BaTiO_3$'s electronic band structure and charge distribution, which are fundamental for photocatalysis. It aids in determining bandgap energies and evaluating charge transfer mechanisms, crucial for understanding photoinduced electron-hole separation in water splitting applications [64–69]. Additionally, defect formation energy calculations using DFT help assess the impact of oxygen vacancies, which play a

 doi:10.20944/preprints202506.0553.v1

critical role in tuning $BaTiO_3$'s optical and electronic response for enhanced photocatalytic performance.

To complement DFT, ab initio MD simulations provide a temperature-dependent and dynamic perspective on $BaTiO_3$'s behavior in aqueous environments or under irradiation conditions. Ab initio MD simulations helps investigate surface interactions, the stability of adsorbed water molecules, and proton transfer mechanisms, which are essential for assessing $BaTiO_3$'s efficiency in photocatalytic water splitting [70–75]. Furthermore, Ab initio MD captures thermal fluctuations and structural rearrangements that static DFT calculations cannot fully describe, offering a more realistic depiction of $BaTiO_3$'s catalytic interface under operating conditions.

In addition, classical all-atom MD simulations provide large-scale insights into $BaTiO_3$ nanoparticle stability, solvent interactions, and ion diffusion in solution-based photocatalytic processes. By employing force field-based molecular dynamics, these simulations help analyze solute-solvent interactions, charge carrier mobility, and ion adsorption at $BaTiO_3$ surfaces [72–80]. This is particularly important for studying $BaTiO_3$-based hybrid photocatalysts, where interactions with co-catalysts, organic molecules, or electrolyte species significantly influence performance.

By integrating DFT, ab initio MD, and classical all-atom MD simulations, researchers can develop a multi-scale understanding of $BaTiO_3$'s photocatalytic properties. This combined approach not only aids in optimizing $BaTiO_3$'s electronic and structural features but also guides the design of novel photocatalytic systems for applications in hydrogen production, CO_2 reduction, and environmental remediation.

1.4. Outline of Our Review

This work presents a topical and characteristic analysis of recent computational studies on $BaTiO_3$-based photocatalysts for solar water splitting. There were various work conducted for atomistic study of advanced energy materials including fuel cells, batteries, hydrogen fuel storage, carbon capture, drug design and others [81–100]. Computational modeling and simulation techniques have become essential tools for examining the electronic structure, defect dynamics, charge transport, and reaction mechanisms of $BaTiO_3$ in photocatalytic applications.

Several computational approaches are commonly utilized in this field:

DFT calculations offer critical insights into the band structure, density of states, charge transfer processes, and defect formation energies [101–110] of $BaTiO_3$. These studies assist in identifying optimal doping strategies to enhance photocatalytic performance.

Ab initio MD simulations are used to investigate the thermal stability, charge carrier dynamics, and interfacial interactions [111–120] of $BaTiO_3$ in aqueous environments under realistic conditions. Ab initio MD provides valuable data on the time evolution of atomic-scale processes.

Classical all-atom MD simulations help analyze the structural and solvation characteristics [121–125] of $BaTiO_3$ surfaces in water. These simulations offer insights into surface adsorption behavior, charge transfer dynamics, and the mechanisms underlying the water-splitting reaction.

To the best of our knowledge, a comprehensive review integrating these atomistic simulation techniques for $BaTiO_3$ photocatalysis remains scarce. This work aims to introduce these computational methods and highlight their recent applications in studying $BaTiO_3$-based solar-driven water splitting.

The discussions in this paper are illustrative, and the examples provided are representative. We believe this review will serve as a valuable resource for researchers focused on designing and optimizing $BaTiO_3$ photocatalysts, encouraging the adoption of DFT, ab initio MD, and classical all-atom MD simulations to explore material properties across different length and time scales.

2. Main Body

2.1. DFT Calculations

 doi:10.20944/preprints202506.0553.v1

DFT calculations serve as a cornerstone for investigating the electronic structure and energetic properties of $BaTiO_3$ -based systems. By solving the Kohn-Sham equations under various approximations for exchange-correlation functionals, DFT provides detailed insights into charge distribution, density of states, and interaction energies at the atomic scale [126–135]. Despite its accuracy, conventional DFT calculations can be computationally demanding, especially for large systems or complex defect structures. To address this, hybrid functionals and dispersion corrections are often incorporated to enhance accuracy, while computational efficiency is improved through localized basis sets and advanced numerical techniques. In this regard, a series of DFT studies in the field of photocatalytic water splitting for $BaTiO_3$-based systems is reviewed below paragraphs and Table 1.

Yang et al. investigated the electronic properties and photocatalytic performance of TiO_2, TiO_2@$BaTiO_3$, and TiO_2@$BaTiO_3$/CdS composites [138]. DFT calculations revealed that pure TiO_2 has a band gap of 3.22 eV, with CB and VB primarily composed of O(p) and Ti(d) orbitals, respectively. Incorporating $BaTiO_3$ reduced the band gap to 1.53 eV while maintaining similar CB and VB compositions. Further modification with CdS introduced slight crystal distortion in $BaTiO_3$, leading to spontaneous polarization and a further reduced band gap of 1.19 eV. The built-in electric field within the $BaTiO_3$ shell facilitated efficient charge separation, enhancing photocatalytic hydrogen evolution. The optimized TiO_2@$BaTiO_3$/CdS nanocomposite exhibited a significantly higher hydrogen evolution rate (13.22 mmol/g·h) and prolonged charge carrier lifetime (0.42 ns), outperforming its individual components and binary composites. This study highlights the potential of ferroelectric photocatalysts in improving charge separation and promoting photocatalytic efficiency.

The study by Cai et al. highlights the synergistic effect of oxygen vacancies and piezoelectric properties in enhancing the photocatalytic CO_2 reduction performance [139] of $BaTiO_3$. By introducing oxygen vacancies, the visible light absorption range was extended, and the density of active surface sites increased, significantly improving charge separation. The piezoelectric effect further facilitated electron-hole separation, enhancing the photocatalytic efficiency.Among the synthesized $BaTiO_3$-X samples, $BaTiO_3$-1.5 exhibited the highest CO production, achieving 6.41 $\mu mol \cdot g^{-1}$ under light alone and 9.17 $\mu mol \cdot g^{-1}$ under light and ultrasound, outperforming pristine $BaTiO_3$ by factors of 3.22 and 1.86, respectively. DFT calculations revealed that oxygen vacancies reduced the band gap from 3.058 eV to 2.717 eV, improving charge transfer. These findings suggest that defect engineering, combined with piezoelectric effects, offers a promising strategy for optimizing $BaTiO_3$-based photocatalysts for CO_2 conversion, with potential applications in sustainable energy solutions.

Wang et al. used first-principles DFT calculations to investigate how non-metal dopants (X = C, Si, N, P, S, Se, F, Cl, Br, I) [140] affect the geometric and electronic structures (Figure 4), stability, and photocatalytic properties of $BaTiO_3$. They examined two doping scenarios: substitution at the oxygen site (X@O) and the titanium site (X@Ti).Their findings align with experimental data, particularly regarding band gap narrowing in N-doped $BaTiO_3$. The preferred doping site depends on the dopant's ionic size and electronegativity. C@O and I@O doping extended absorption into the visible spectrum, enhancing photocatalytic efficiency, while S and Se doping at either site improved photo-oxidation and photo-reduction.F- and N-doped $BaTiO_3$ (X@O) and Si-doped $BaTiO_3$ (X@Ti) were thermodynamically favorable. The study supports previous theories, highlighting non-metal doping's role in modifying $BaTiO_3$ for visible-light photocatalysis, with further experimental validation needed.

 doi:10.20944/preprints202506.0553.v1

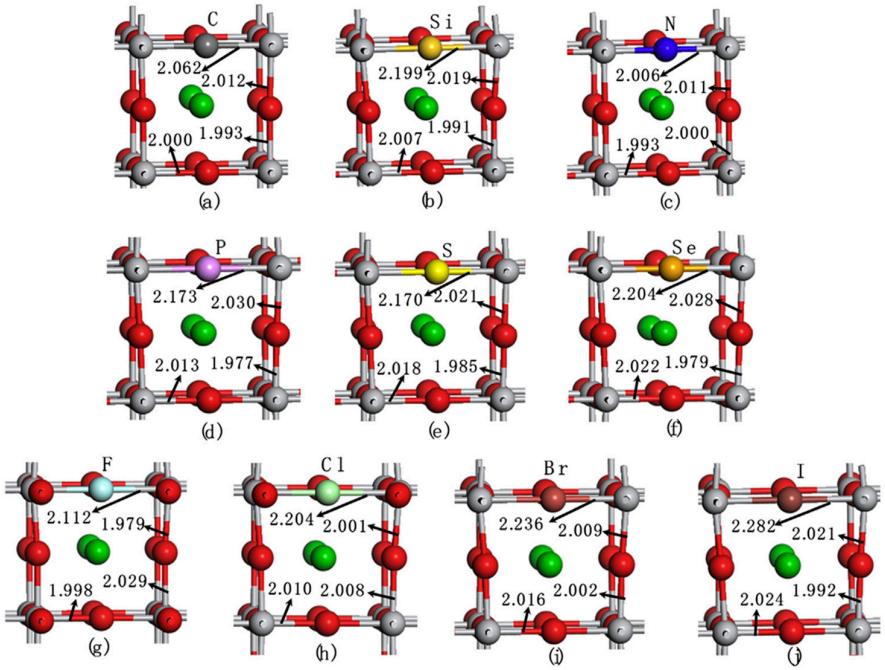

Figure 4. Optimized local structures of $BaTiO_3$ configurations doped with (a) C, (b) Si, (c) N, (d) P, (e) S, (f) Se, (g) F, (h) Cl, (i) Br, and (j) I, where X substitutes O (X@O).Reprinted with permission from [140]. Copyright 2019, for Elsevier.

Table 1. Recently performed DFT calculation details and main findings.

Designed systems	Methods	Main findings
TiO_2[138]	DFT calculations using VASP with GGA-PBE functional. PAW method for ion-electron interactions (cutoff energy: 400 eV). DFT+U approach for d-electron correlation correction. FDTD method for electric field distribution simulations.	Calculated band gap of TiO_2: 3.22 eV. Conduction band (CB) primarily composed of O(p) orbitals. Valence band (VB) primarily composed of Ti(d) orbitals. Photogenerated charge likely accumulates in these orbitals.
TiO_2@ $BaTiO_3$[138]		After combining with $BaTiO_3$, CB and VB compositions remain similar to TiO_2. Calculated band gap decreases to 1.53 eV (approximately half of TiO_2). Adding CdS clusters to TiO_2@$BaTiO_3$ caused slight crystal distortion in $BaTiO_3$, potentially inducing spontaneous polarization.
TiO_2@ $BaTiO_3$/ CdS [138]		Density of states at CB and VB formed by S(p), Ba(d), and Cd(d) orbitals. Band gap further decreased to 1.19 eV. TiO_2@$BaTiO_3$/CdS nanosheet exhibits an intrinsic electric field, facilitating charge separation and diffusion to the surface.
Wheat-heading $BaTiO_3$ [139].	DFT calculations using Materials Studio 2017 GGA-PBE functional Plane wave cutoff energy: 400 eV K-point mesh: 3 × 3 × 3 Maximum force tolerance: 0.05 eV/Å Cleaved along [001] direction Vacuum thickness of 10 Å in z-direction	Band gap for wheat heading $BaTiO_3$: 3.058 eV CB mainly composed of Ti 3d and O 2p orbitals VB dominated by O 2p orbitals Charge transfer from O 2p to Ti 3d
Wheat-heading BaTiO3-Oxygen Vacancy (Ovs) [139]		After oxygen vacancy, band gap reduced to 2.717 eV VB remains dominated by O 2p orbitals CB contributions shift to O 2p, Ba 3d, and Ti 3d Enhanced charge transfer between Ti and Ovs Higher charge density improves piezo-photocatalytic performance
Pure $BaTiO_3$[140]	Spin-polarized DFT calculations using VASP GGA-PBE functional	Structural and electronic properties of $BaTiO_3$ were well reproduced

 doi:10.20944/preprints202506.0553.v1

	PAW method for core electrons Plane-wave cutoff energy: 400 eV 9 × 9 × 9 Monkhorst-Pack k-point mesh Fully optimized cubic $BaTiO_3$ unit cell with a lattice parameter of 4.004 Å 2 × 2 × 2 supercell (40 atoms) modeled for bulk $BaTiO_3$ Geometry convergence criterion: forces < 0.01 eV/Å HSE06 functional for electronic structure calculations with HF exchange fraction (α) = 0.32	Band gap improved with HSE06functional, aligning with experimental values Basis for further doping studies to enhance photocatalytic properties F- and N-doped $BaTiO_3$ (X@O) and Si-doped $BaTiO_3$ (X@Ti) showed negative formation energy, indicating thermodynamic stability Stability of doping systems depends on ionic radius and electronegativity of dopants relative to O or Ti C-, S-, Se-, and I-doped $BaTiO_3$ (X@O) extended the absorption edge into the visible light region, enhancing photocatalytic water splitting capabilities S- and Se-doped $BaTiO_3$ (X@Ti) exhibited potential for water splitting under visible light
Non-metal-doped $BaTiO_3$ (X@O or X@Ti, X = C, Si, N, P, S, Se, F, Cl, Br, I) [140]	DFT calculations with VASP 3 × 3 × 3 k-point mesh for geometry optimization and electronic properties Substituting O or Ti with non-metal dopants at a doping concentration of 2.5 at.% HSE06 functional used for accurate band gap calculations	Doping-induced modifications improved both photo-oxidation and photo-reduction properties of $BaTiO_3$ Key Findings for X@O Doping Band gap (Eg) range: 1.93 eV (C) – 3.31 eV (Si, P, F) Highest CBM: F-doped $BaTiO_3$ (-3.82 eV) Lowest CBM: Si-doped $BaTiO_3$ (-3.03 eV) Electronegativity (χ) range: 4.68 (Si) – 5.47 (F) Photocatalytic potential: C-, S-, Se-, and I-doped $BaTiO_3$ extend absorption into the visible region, enhancing photocatalytic efficiency. Key Findings for X@Ti Doping Band gap (Eg) range: 0.84 eV (Cl) – 3.31 eV (F) Narrowest band gap: Cl-doped $BaTiO_3$ (Eg = 0.84 eV), due to low CBM (-5.69 eV) and VBM (-6.53 eV) Highest CBM: Si-doped $BaTiO_3$ (-3.89 eV) Highest VBM: Br-doped $BaTiO_3$ (-7.47 eV) Electronegativity generally higher for X@Ti systems compared to X@O, resulting in distinct electronic structure modifications.
Pure $BaTiO_3$[141] La-doped $BaTiO_3$[141]	CASTEP program in Materials Studio DFT with plane-wave pseudopotential method GGA-PBE functional Birch-Murnaghan equation of state for lattice optimization Cut-off energy: 340 eV	$BaTiO_3$ exists in a cubic structure (Pm3m) with Ba at corners, Ti at the body center, and O at face centers. The calculated lattice constant is 4.034 Å, closely matching experimental values. Optical properties such as dielectric function, absorption, and refractive index are analyzed. La doping at Ba sites reduces the lattice parameter (a = 3.971 Å) and unit cell volume. The band structure changes from an indirect to a direct band gap, reducing the gap to 1.569 eV. This shift enhances conductivity by facilitating electron-hole recombination. The La-5d states contribute significantly to the conduction band. Optical properties, including dielectric function, absorption, and refractive index, are modified.
$BaTiO_3$ with Ba and Ti vacancy [142]	Modeled using Materials Studio Optimized structure using VASP First-principles calculations based on DFT framework 2 × 2 × 2 crystal structure containing 8 Ba, 24 O, and 8 Ti atoms	Lattice distortion occurs due to Ba and Ti vacancies, affecting oxygen coordination and Coulomb repulsion. Oxygen vacancies are necessary for charge conservation in the system.

 doi:10.20944/preprints202506.0553.v1

	PAW and PBE methods used for structure optimization and charge density calculations	Lattice expansion and distortion due to Ti and O vacancies are significantly higher than those caused by Ba and O vacancies. Charge density changes: • Ba and O vacancies decrease charge density in specific regions of the unit cell. • Ti vacancy increases and homogenizes charge density at the vacancy position. Lattice deformation leads to internal atomic shifts, with Ti atoms moving away from symmetry centers.
Pure $BaTiO_3$ (BTO) [143] Mo-doped BTO (2.5 at%) [143]	First-principles calculations using DFT with the supercell approach, performed using VASP. Functional: Generalized Gradient Approximation (GGA) for the projector-augmented wave (PAW) method. Structural Model: Cubic 1×1×1 BTO unit cell. Plane-wave energy cutoff: 500 eV. k-point sampling: Monkhorst-Pack grid of 7×7×7.	The calculated bandgap of pure BTO is 1.56 eV, which is underestimated due to DFT limitations. Charge-density analysis confirms covalent Ti–O bonding. Mo doping narrows the bandgap to 1.27 eV due to impurity levels formed by Ti 3d and Mo 3d interactions. Mo–O bonding results in a more uniform charge distribution than pure BTO.
Pure $BaTiO_3$ [144] Cs-doped $BaTiO_3$ (0.13%, 0.26%, 0.39%) [144]	• CASTEP code used for geometry optimization and property investigation. • GGA-PBE exchange correlation functional with DFT+U correction (U = 4 for Ti-d orbital). • Plane-wave pseudopotential technique based on DFT. • Vanderbilt-type ultrasoft pseudopotentials for electron–ion interactions. • BFGS energy minimization for electronic wave functions and charge densities. • Pulay density mixing scheme applied. • Monkhorst–Pack method for k-point sampling (6×6×6 k-points mesh). • Energy cutoff = 630 eV. • Total energy difference per atom: 2×10^{5} eV. • Max ionic displacement: 2×10^{3} Å. • Cubic phase (Pm3m, 221) chosen.	Pure $BaTiO_3$ Indirect band gap: 2.513 eV (higher than previous theoretical value of 1.719 eV but closer to experimental results). The difference is due to DFT+U correction, as earlier studies used only PBE-GGA. TDOS maximum peak at 4.29 eV (6.58 value), with other peaks at 1.79 eV and 0.95 eV. Phonon spectra show no imaginary frequencies, confirming stability. For Cs-doped $BaTiO_3$ (0.13%, 0.26%, 0.39%) Band gap converts from indirect to direct upon Cs doping. 0.13% Cs: 1.858 eV (direct band gap). 0.26% Cs: 2.103 eV (direct band gap). 0.39% Cs: 1.882 eV (direct band gap). TDOS of 0.13% Cs-doped $BaTiO_3$ shows enhanced peaks, with a maximum peak at 0.77 eV (57.46 value). New peaks in TDOS appear at 3.43, 2.37, 2.40, 3.36, and 4.47 eV. Phonon spectra confirm stability for 0.13% Cs-doped $BaTiO_3$ (no imaginary frequencies detected).
$BaTiO_3$(111) surfaces with different terminations [145]	DFT calculations using VASP PAW method for core electrons Plane-wave basis with 400 eV cutoff DFT+U approach with PBE functional (Ueff = 4.0 eV for Ti 3d) Conjugated gradient geometry optimization 6×6×1 Monkhorst-Pack k-point sampling Dipole correction applied Slab model with 13 atomic layers (7 fixed, 6 relaxed) and 15 Å vacuum gap Considered stoichiometric (BaO_3, Ti) and non-stoichiometric (BaO_2, BaO, Ba, O_3, O_2, O) terminations	Surface energy and stability BaO_2 and O terminations have the lowest cleavage energies, making them the most thermodynamically stable. Removal of oxygen, Ti, or Ba reduces cleavage energy, stabilizing polar surfaces. Excess Ba (BaO +O_2) or oxygen (Ba +O_3) leads to instability with higher cleavage energies. Phase diagram analysis (SGP method) BaO_2 and O terminations dominate under wide O- and Ba-rich conditions. Stoichiometric BaO_3 and Ti terminations are stable only in limited conditions. Results from O-Ti phase diagram match O-Ba phase diagram, confirming BaO2 and O as the most stable. Charge compensation mechanism Bader charge analysis shows charge redistribution in surface layers to compensate dipole moments.
$BaTiO_3$ doped with chalcogens (S, Se, Te) under different concentrations [146]	DFT calculations using WIEN2K package with FP-LAPW method and LDA+mBJ exchange-correlation potential Calculation of $\varepsilon(\omega) = \varepsilon1(\omega) + i\varepsilon2(\omega)$	$BaTiO_3$ has a cubic Pm3m structure. Lattice constant (a0 = 3.9412 Å) agrees with experimental (4.0000 Å) and theoretical values. The forbidden band gap decreases with increasing chalcogen concentration due to electronegativity differences. Doping reduces the band gap significantly (Eg reduction from 2.901 eV to 0 eV in some cases).

 doi:10.20944/preprints202506.0553.v1

Pressed $BaTiO_3$ (2.3% axial compressive strain)[147] Barium Titanate under triaxial compressive strain [147]	- Ab initio calculations based on DFT using FP-LAPW method (WIEN2K package) - Exchange correlation potential: LDA + mBJ - Thermoelectric properties: BoltzTraP code - Brillouin zone integration: 6×6×6 k-points for electronic and optical properties, 10×10×10 for thermoelectric properties - Structural optimization: Comparison with experimental and theoretical results	Strong hybridization occurs between O-2p and chalcogen-p orbitals. Lattice constant reduced to ap = 3.8505 Å. Pressed BaTiO3 exhibits a direct bandgap at the Γ point, unlike pure BaTiO3, which has an indirect bandgap. Further band gap reduction compared to non-pressed doped structures. Pressed BaTiO3 exhibits slightly higher optical property peaks in ε1(ω) and ε2(ω) compared to pure BaTiO3. Electronic properties: Pure BaTiO3 is a semiconductor with an indirect band gap (2.901 eV for cubic, 2.922 eV for tetragonal phase) Under ξ = 2.3% compressive strain, BaTiO3 transitions to a direct band gap semiconductor, improving potential for photovoltaic applications Density of States analysis confirms VB is mainly O-2p, while CB is Ti-3d Band gap increases with strain, indicating possible piezoelectric properties
$BaTiO_3$ (001) surfaces doped with metal and nonmetal elements [148]	DFT calculations using VASP, PBE functional under GGA, and HSE06 hybrid functional. Plane-wave cutoff energy: 400 eV. k-point mesh: 9×9×9 for bulk optimization and 3×3×1 for surface calculations.	The tetragonal $BaTiO_3$ unit cell was fully optimized, with lattice parameters a = b = 3.992 Å, c = 4.056 Å, matching experimental and theoretical results. $BaTiO_3$ (001) surface modeled with TiO_2- and BaO-terminations. Symmetric slabs (odd atomic layers) were adopted due to the absence of macroscopic dipole moments. Co-doped systems (M+X) are more stable when M and X are adjacent due to M-X bond formation. Formation energies indicate that O substitution by C or N is easier under Ti-rich conditions, while Ti substitution by metal dopants is favored under O-rich conditions. Binding energy calculations show that co-doped systems are more stable than mono-doped systems. The computed bandgap of bulk $BaTiO_3$ is 3.03 eV, while the pure $BaTiO_3$ (001) surface has a bandgap of 1.42 eV. Passivated co-doping (e.g., V+N, Nb+N, Ta+N) introduces charge compensation, eliminating mid-gap states. The Ta+N co-doping system leads to the most significant bandgap narrowing (1.09 eV) due to the upshift of the valence band maximum.
$BaTiO_3$ polymorphs (Cubic, Rhombohedral, Orthorhombic, Tetragonal, Hexagonal) [149]	First-principles calculations using CASTEP within DFT framework (GGA-PBE, LDA, and HSE06 functionals)	Optimized lattice parameters are consistent with theoretical and experimental results. Formation enthalpies indicate all phases are energetically stable, with cubic phase being the most stable. Band structure analysis shows indirect bandgaps for four phases and a direct bandgap for the hexagonal phase. GGA-PBE and LDA underestimate bandgaps, while HSE06 gives values closer to experimental data. Higher electron mobility and conductivity inferred from band structure analysis. Density of states analysis confirms structural stability and electrical conductivity.
$BaTiO_3$, PGBT [150] $BaTiO_3$, PG, PGBT [150]	Electronic structure and density of states calculations using Quantum ESPRESSO with PBE pseudopotentials - k-mesh: 9 × 9 × 1 for self-consistent field (scf) and 18 × 18 × 1 for non-self-consistent field calculations. - Energy cutoff: 90 Ry for wavefunctions, 740 Ry for charge density.	Redshift in absorption edges of PGBT compared to pure $BaTiO_3$. Bandgap energies (Tauc method): $BaTiO_3$ (3.12 eV), PGBT (2.95–2.79 eV, decreasing with increasing PG content). Lower fluorescence intensity indicates reduced charge carrier recombination, enhancing photocatalytic efficiency. Electron migration from $BaTiO_3$ to PG via Ba–C bond supports charge separation. Beyond 7.5 PGBT, fluorescence intensity increases due to excess PG acting as a recombination center. Fully relaxed 5 × 5 × 1 supercell of PGBT with a 12 Å vacuum to prevent interaction between composites. Estimated bandgap of 1.74 eV (indirect, R to Γ), lower due to DFT underestimation.

 doi:10.20944/preprints202506.0553.v1

$Ba_{1-x}Ga_xTiO_3$ (x = 50%) [151]	DFT simulations using WIEN2k Tetra-elastic package for elastic properties $Ba_{1-x}Ga_xTiO_3$ was studied using full-potential linearized augmented plane wave (FP-LAPW) method. A 2000 k-point mesh was used for Brillouin zone integration. Band structure and density of states were analyzed for electronic properties. Elastic coefficients were calculated usingEulerian strain approach. The unit cell structure was modeled with tetragonal symmetry.	Additional bandgaps observed: direct at Γ, indirect from M to Γ. $BaTiO_3$: VB primarily from O 'p' states; CB dominated by Ti 'p' states with minor O 'p' contributions. Pristine $BaTiO_3$ exhibits an indirect band gap of 2.65 eV. Ga substitution reduces the band gap to 1.84 eV for the majority spin channel. The minority spin channel exhibits metallic behavior with a half-metallic gap of 0.59 eV. Partial density of states analysis shows significant contributions from O-p, Ti-d, and Ga-p states. Dielectric constant ($\varepsilon_1(0)$) increased from 8.8 (pure) to 100 (Ga-doped). A peak in the imaginary dielectric function $\varepsilon_2(\omega)$ at 3.9 eV corresponds to O-p electron transitions to the conduction band. Ga doping shifts absorption peaks towards the visible and infrared regions, enhancing optical activity.
t-BTO@NiFe-LDH heterojunctions [152]	First-principles DFT calculations within GGA using PBE functional PAW potentials for ionic cores Plane wave basis set with 450 eV cutoff Gaussian smearing (0.05 eV) Self-consistent energy threshold: 10^{-6} eV Geometry optimization convergence: 0.05 eV/Å 2 × 2 × 1 Monkhorst-Pack k-point sampling Adsorption energy (E_ads) and free energy (G) calculations	Formation of t-BTO@NiFe-LDH heterojunctions increased Ni^{3+} content (45% → 68% for NiFe LDH, 61% → 83% for t-BTO@NiFe-LDH) after OER test. Fe^{3+}/Fe^{2+} ratio increased slightly after OER test, improving OER electrocatalytic activity. Free energy calculation showed a lower rate-determining step (RDS) energy for t-BTO@NiFe-LDH (1.52 eV for Ni site, 1.76 eV for Fe site) compared to NiFe-LDH. Bandgap of t-BTO@NiFe-LDH (0.42 eV) was lower than NiFe-LDH (0.95 eV) and t-BTO (2.37 eV), indicating enhanced electronic conductivity. Charge density difference analysis showed electron transfer from NiFe-LDH to t-BTO, improving OER activity. d-band center shifted from 3.89 eV (NiFe-LDH) to 2.98 eV (t-BTO@NiFe-LDH), favoring adsorption of OER intermediates. Enhanced electron movement near Ti atoms improved spontaneous polarization of t-BTO.
BTO, BTPO-0.09, BTPOv-0.09 [153]	DFT using VASP PBE exchange-correlation function PAW pseudopotentials Cutoff energy: 520 eV Monkhorst-Pack 2×2×1 k-points for Brillouin zone sampling DFT-D3 for vdW interactions Geometry optimization criteria: 1.0×10^{-5} eV/atom (energy), 0.01 eV/Å (force) UV-Vis diffuse reflectance spectroscopy UV photoelectron spectroscopy Electrochemical impedance spectroscopy XANES and XPS for charge distribution analysis	The bandgaps of synthesized materials (3.24 eV, 3.20 eV, and 3.13 eV) are close to theoretical values, confirming minimal influence from PtOx loading. Pt-O-Ti^{3+} sites act as defect energy levels and oxidation sites. Charge density analysis revealed electron accumulation around PtOx and depletion around Ti atoms, matching XANES and XPS results. Polarization studies showed improved current response for PtOx-loaded samples, confirming enhanced photocatalytic activity. Pt serves as an electron aggregation center, accelerating proton reduction for H_2 production. Oxygen vacancies facilitate charge aggregation, and Ti^{3+} defects enhance rapid electron transfer. The defect energy level at Pt-O-Ti^{3+} sites allows efficient separation of electrons and holes, leading to an effective bifunctional catalytic system.
$BaTiO_3/SrTiO_3$ [154]	First-principles calculations using DFT-D3 VASP Generalized-Gradient Approximation (GGA) with PBE functional Kinetic cutoff energy: 520 eV Brillouin zone sampling: 5×5×1 Monkhorst-Pack mesh External electrostatic field along [001] direction (E = 0.1 eV/Å) Band structure and density of statescalculations Gibbs free-energy change (ΔG_H*) calculations for hydrogen adsorption Visualization with VESTA software	The $BaTiO_3/SrTiO_3$ heterojunction has a lower bandgap (1.1 eV) compared to individual $SrTiO_3$ (2.31 eV) and $BaTiO_3$ (2.15 eV), promoting photocatalytic efficiency. Application of an external electric field further narrows the bandgap to 1.0 eV, enhancing electron transport and energy band bending. Differential charge density analysis reveals efficient electron transfer from $BaTiO_3$ to $SrTiO_3$ at the heterostructure interface. Hydrogen adsorption Gibbs free energy (ΔG_H*) shows $SrTiO_3$ (0.57 eV), $BaTiO_3$ (-1.01 eV), and $BaTiO_3/SrTiO_3$ (-0.42 eV), indicating $BaTiO_3/SrTiO_3$has optimized adsorption-desorption balance.

 doi:10.20944/preprints202506.0553.v1

Zr+X codoped $BaTiO_3$ systems [155]	DFT calculations SCAN functional for structural and energetic properties TB-mBJ functional for electronic and optical properties Full-potential linearized augmented plane wave (FP-LAPW) method using WIEN2k package 2×2×2 supercell approach for constructing doped and codoped systems k-mesh: 12×12×12 for bulk, 6×6×6 for supercell	Structural and Thermodynamic Properties: SCAN functional accurately predicts lattice parameters and cohesive energies. The computed cohesive energies of S, Se, and Te match well with previous studies. Electronic Properties: TB-mBJ functional predicts larger band gaps than SCAN functional. X-doped systems (BTOX) have valence band edges composed of O-2p states with contributions from X-p states. Zr-doped system (BTZO) shows conduction band modifications due to Zr-4d states. Zr+X codoping (BTZOX) leads to a reduced band gap, making them promising for visible-light applications.
MO/BTO Heterostructures (ZnO/BTO, TiO2/BTO, SnO2/BTO) [156]	DFT using QuantumEspresso GGA for exchange-correlation functional Plane wave basis (320 Ry cut-off) k-point meshes: 6×6×1 for integration, 12×12×1 for density of states Marzari-Vanderbilt cold smearing (0.05 Ry) Fully relativistic norm-conserving pseudopotentials van der Waals corrections included DFT+U for accurate band gap predictions Charge carrier effective masses calculated from Bloch band curvature Structural relaxations using BFGS algorithm	Structural Properties: ZnO/BTO shows a decrease in BTO lattice vector c due to interface-induced tetragonality enhancement. Interface distances: ZnO/BTO (2 Å), TiO2/BTO and SnO2/BTO (4 Å). ZnO mid-slab oxygen layers exhibit large displacements due to interface interactions. Lattice mismatch effects cause strain in BTO, compressing c in ZnO/BTO. Electronic Properties: Band gaps in bulk: BaTiO3 (3.28 eV), ZnO (3.41 eV), TiO2 (3.17 eV), SnO2 (3.52 eV). Interface effects modify band structures, introducing metal-induced gap states in ZnO/BTO. ZnO/BTO exhibits highly dispersive bands due to stronger interface interaction. TiO2/BTO shows a single dispersive surface state, SnO2/BTO retains bulk-like band structure. BTO and SnO2 maintain their direct semiconducting nature in HS form.
Rhombohedral $BaTiO_3$ ($BaTiO_3$ (001) surface, pure and Rh-doped) [157]	Ab initio plane-wave calculations using VASP with PAW formalism and PBE-GGA exchange-correlation functional. Solvation effects modeled using VASPsol. Monkhorst–Pack grid: 2×2×2 for bulk, 2×2×1 for slab. Cutoff energy: 520 eV. Convergence tolerance: 10^{-6} eV. Slab models with 7 alternating TiO_2- and BaO-planes and 13 Å vacuum gap. Rh doping effects analyzed by replacing Ti with Rh and re-optimizing structures.	Rhombohedral $BaTiO_3$ is ferroelectric and stable below 90°C. Structural calculations show good agreement with experimental and previous theoretical studies. Ti displacement (-0.0137 Å) and O displacement (0.0232 Å) along [111] in rhombohedral $BaTiO_3$. Calculated Ba–O (2.87 Å) and Ti–O (1.89 Å) bond lengths match experimental data. Direct bandgap of 2.25 eV is consistent with previous theoretical studies, though underestimated by GGA-PBE. $BaTiO_3$ (001) surface (TiO_2-terminated) is nonpolar with a vacuum gap of 13 Å in slab models. Rh doping (substituting Ti with Rh) slightly affects lattice structure; minimal bond length change observed. Effective charge of Rh (1.66e) is lower than Ba (2.55e). Rh doping reduces the bandgap from 1.45 eV to 0.67 eV and introduces an in-bandgap acceptor level (0.115 eV above Fermi level). Rh and O hybridized orbitals create defect states in the bandgap, influencing photocatalytic performance.
$BaTiO_3$/$LaAlO_3$ heterostructures [158]	DFT calculations using Quantum Espresso Norm-conserving pseudopotentials GGA-PBE functional for exchange-correlation Monkhorst-Pack k-point grid (10×10×1 for heterostructure, 12×12×1 for bulk) 30 Å vacuum space with dipole correction DFT-D3(BJ) for van der Waals interactions Plane-wave cut-off energy: 45 Ry Slab model for surface and interface calculations Geometry optimization using the BFGS scheme Self-consistent field iteration convergence: 10^{-6} Ry	Optimized lattice parameters of bulk $LaAlO_3$ (3.83 Å) and $BaTiO_3$ (3.97 Å) agree with experimental values. Small lattice mismatch (-3.16%) in Conf(001) heterostructure allows epitaxial growth. Lattice mismatch in Conf(011) and Conf(111) was reduced using supercell stacking. Ab initio MD and phonon dispersion results confirm dynamic and thermal stability of $BaTiO_3$/$LaAlO_3$(001) heterostructures at 300 K. $BaTiO_3$(001) surface has the lowest bandgap (3.44 eV), favoring higher photocatalytic performance. $BaTiO_3$(011) and (111) surfaces show direct bandgap behavior (4.05 eV, 3.75 eV). Conf(111) heterostructure has an indirect bandgap (1.59

 doi:10.20944/preprints202506.0553.v1

	Hybrid HSE06 functional for electronic structure calculations	eV), while Conf(011) and Conf(111) show direct bandgap (2.21 eV, 1.75 eV), making them promising for visible-light photocatalysis. PDOS analysis reveals that charge carrier separation efficiency is influenced by surface composition.
$BaTiO_3$ thin films with TiO_2- and BaO-terminated slabs for electrocatalysis [159]	Ab initio periodic DFT+U calculations using the Quantum Espresso package, with GGA+U approximation and ultrasoft pseudopotentials. U = 4 eV for Ti d states. Kinetic energy cutoff: 320 eV. K-point grids: 4 × 4 × 1. Slabs modeled with four BaO and four TiO_2 layers on Pt as an electron reservoir. Binding free energy calculations performed for HER mechanism.	Polarization direction affects electronic structure: Upward polarization → Electron-rich surface (downward band bending, Ti d states near Fermi level). Downward polarization → Hole-doped surface (upward band bending, O p states near Fermi level). Surface energy calculations: TiO_2-terminated slabs are the most stable. HER activity trends: Poled-up surfaces show smaller reaction barriers for HER, making them more favorable. Only H adsorption on O site of poled-down surface has an optimal
Up-poled and Down-poled BFO/BVO heterostructures [160]	DFT calculations using CRYSTAL23 code with B3LYP functional, D3 dispersion corrections, and spin polarization. Basis sets: pob-TZVP-Rev2. Slabs modeled in R3c space group with (110) surface exposed.	Up-poled BFO surface: Spontaneously dissociates water molecules, converting surface O to OH. Oxygen vacancies migrate to the surface under upward polarization, enhancing OH adsorption. XPS spectra: OL-H peak intensity increases, OL peak weakens and broadens with blue shift due to electron transfer to BVO. Stronger interaction with water compared to down-poled BFO, enhancing OW-C and OW-P peaks. Binds molecular oxygen more strongly, which may slow reaction rate. Down-poled BFO surface: H+ adsorption promotes surface OH formation, enhancing OL-H peak. OL and OL-H peaks shift to higher binding energies due to ferroelectric polarization effects. Weaker interaction with water, dominated by physisorption, leading to weaker OW-C peak and stronger OW-P peak. More fluid interaction with water and easier oxygen desorption, improving reaction rate. pH significantly affects BFO-water interactions due to availability of H+/OH−.
Anionic mono- and co-doped $BaTiO_3$[161]	QuantumATK software package DFT with PBE-GGA Norm-conserving PseudoDojo pseudopotential Self-consistent field simulations (10^{-8} Ha tolerance LBFGS geometry optimization Monkhorst–Pack k-grid for Brillouin Zone integration HSE06 hybrid density functional for electronic calculations 2×2×2 supercell approach with periodic boundary conditions	Lattice constants of mono-doped and co-doped $BaTiO_3$ structures decrease due to incorporation of anionic elements. Formation energy calculations indicate anionic co-doping is more stable than mono-doping, especially in O-poor conditions. N-doping introduces asymmetrical density of state, leading to magnetic behavior (+1.0 μB). P-doping also induces magnetism (+1.0 μB) and localized states near the Fermi level. C-doping introduces two acceptor levels, with a strong magnetic moment (+2.002 μB). S-doping maintains valence electron count, interacting with Ti 3d states and resulting in a favorable band gap (2.24 eV) for visible light absorption. Co-doped systems (e.g., N-N, C-S, N-P) exhibit lower formation energies than their mono-doped counterparts, making them more thermodynamically favorable. N-N co-doping is the most stable due to similar atomic radii and strong anionic interactions.
Ir-doped $BaTiO_3$ [162]	DFT calculations usingVASP Projector Augmented Wave (PAW) method Generalized Gradient Approximation (GGA) with Perdew–Burke–Ernzerhof (PBE) functional GGA+U method (U values: Ti = 4 eV, O = 8 eV, Ir = 2 eV) Self-consistent and non-self-consistent field calculations with Monkhorst–Pack k-point grids (3×3×3 and 7×7×7)	Ir doping at the Ti site in BTO induces a transition from n-type to p-type conductivity. DOS calculations reveal a substantial downward shift in the Fermi level (from 4.36 eV to 3.18 eV), confirming p-type behavior. Ir doping at the Ba site does not induce a similar Fermi-level shift. DOS analysis indicates partially and fully occupied Ir 5d orbitals below and above the Fermi level.

 doi:10.20944/preprints202506.0553.v1

	Cutoff energy: 500 eV Structural relaxation criteria: Total energy convergence at 10^{-6} eV, residual atomic force <0.01 eV/Å Analysis of Density of States and Fermi-level shifts	Charge neutrality is maintained by Ir^{3+} to Ir^{4+} transitions, contributing to hole formation and p-type behavior. Findings align with previous studies on Rh-doped $SrTiO_3$. Ir-doped BTO exhibits visible-light absorption, making it a promising material for optoelectronic and photocatalytic applications. urther investigations on solar hydrogen evolution activity are in progress.
Rh-doped BaTiO3 (Case A: Rh at Ba and Ti sites) [163]	- First-principles DFT calculations using Quantum ESPRESSO - PW functional with LDA pseudopotential - Norm-conserving pseudopotential with valence electrons: $6s^2$ (Ba), $3d^24s^2$ (Ti), $2s^22p^4$ (O) - Plane wave cutoff: 120 Ry, charge density cutoff: 480 Ry - k-point mesh: 4×4×4 (SCF), 8×8×8 (NSCF) - Electronic structure along G-X-M-G-R-X path	$BaTiO_3$ has a cubic perovskite structure Direct bandgap of 1.929 eV at G point due to folding of R point onto G point in 2×2×2 supercell Additional indirect bandgap transitions (R → G and M → G) Underestimation of bandgap in DFT due to derivative discontinuities Valence band formed by O p-orbitals, conduction band formed by Ti d-orbitals Ba atoms have an ionic nature and do not contribute significantly to pDOS Rh-doped BaTiO3 (Case A: Rh at Ba and Ti sites) Formation of acceptor level within the bandgap (width: 0.167 eV above Fermi level) Reduction of bandgap to 0.673 eV Acceptor level formed due to hybridization of Rh (Ba site) d-orbitals and O p-orbitals Large gap (1.032 eV) between valence band and acceptor level increases recombination center lifetime Deep defect states observed in wavefunction analysis Direct bandgap: 2.028 eV at G point Indirect bandgap: 1.796 eV (X → G) due to defect band overlapping with valence band edge Hybridization of O p-orbitals and Rh d-orbitals at defect band region Rh-doped BaTiO3 (Case C: Rh at Ba sites only) Formation of donor level (width: 0.363 eV) 0.148 eV above valence band edge Reduction of bandgap to 1.525 eV (lowest among cases) Valence band mainly from O p-orbitals, with hybridization with Rh d-orbitals Minor Rh d-orbital contributions in conduction band Single occupancy ensures continuous band structure, facilitating charge carrier migration
$BaTiO_3$ surfaces with different polarization states for hydrogen evolution reaction [164]	First-principles calculations using VASP 5.4.4 with GGA-PBE functional and DFT-D3 dispersion correction	The tetragonal phase of BTO was used, as it is stable at room temperature where HER occurs. GGA was chosen due to limitations of LDA for hydrogen-bonded ferroelectrics. Lattice constants were fixed to experimental values. The calculated polarization of BTO bulk (30.23 μC/cm²) is close to experimental (~26 μC/cm²), and U_eff = 6 eV improves accuracy. Surface structure relaxation leads to rumpling, affecting adsorption behavior. For out-of-plane polarized BTO, the most stable hydrogen adsorption site is the surface oxygen site. The surface titanium site is inactive for HER. In-plane polarization states can be modulated via thin-film growth techniques and electrochemical poling. A switchable HER catalysis mechanism is proposed, where mechanical strain can modulate BTO polarization states, affecting hydrogen adsorption.
La-N@B co-doped BaTiO3 [165]	DFT computations using CASTEP in Material Studio PBE exchange-correlation functional with GGA + U (U = 4.3 eV for Ti-3d, 8.1 eV for La-4f) Energy cutoff: 500 eV k-point grid: 3 × 3 × 3 Ultra-soft pseudopotentials Energy convergence: 1.0×10^{-5} eV/atom	La and N mono-doping effects: La substitution at the Ba site reduced the bandgap to 1.55 eV La substitution at the Ti site caused a slight bandgap increase (+0.10 eV) N substitution at O sites lowered the bandgap to 1.23 eV Co-doping impact (La-N@B, 25%): Band edge positions were more favorable for photocatalytic water decomposition

 doi:10.20944/preprints202506.0553.v1

	Structural relaxation: Max force = 3.0×10^{-2} eV/Å, Max stress = 5.0×10^{-2} GPa, Max atomic displacement = 1.0×10^{-3} Å	Modulated electronic structure and optimized bandgap for improved absorption properties PDOS and TDOS analysis revealed Ti-3d and O-2p as dominant contributors to the conduction band minimum (CBM) and valence band maximum (VBM) - The cubic BaTiO3 phase (Pm3m) was used as a structural model despite its high-temperature stability for computational feasibility Modeled BaTiO3 (001) surfaces with TiO2- and BaO-terminated slabs. Rh doping of Ba/Ti sites prevents dipole moments due to symmetry preservation.
[57] Tetragonal BaTiO3 with (001) TiO2- and BaO-terminated surfaces	DFT calculations using HSE06 functional Geometry optimization and substitution energy calculations Density of States and optical absorption analysis	BaO-terminated surfaces found to be unstable under operating conditions. Substitution of Ti4+ with Rh4+ slightly distorts the lattice, while Ba2+ → Rh3+ + OH− substitution leads to significant structural changes. Doping the TiO2-terminated surface with Rh4+ introduces Rh-4d states in the band gap, reducing its value. Optical absorption threshold shifts due to Rh4+ doping, with DOS analysis confirming band gap modifications.
[166] Pt-doped $BaTiO_3$	First-principles calculations using the supercell method, DFT with GGA-PW91, CASTEP, PAW approach, Energy cutoff: 300 eV, Monkhorst-Pack k-mesh (4×4×4), Scissor operator (0.75 eV) applied	Optimized $BaTiO_3$ unit cell and constructed 2×2×2 supercell (40 atoms). Pt doping at Ba and Ti sites (0.125 ratio) slightly reduces stability but remains thermodynamically favorable. Bandgap reduction observed: 1.78 eV (Ba site) and 2.06 eV (Ti site), indicating semiconducting behavior. Strong hybridization between Pt–5d and O–2p states. Mulliken charge analysis shows increased charge redistribution around O atoms. Pt doping introduces ferromagnetism in $BaTiO_3$. Charge density analysis confirms the ionic-covalent bonding nature.
BaTiO3/Cu2O heterojunction [167]	Quantum Espresso package DFT Generalized Gradient Approximation (GGA) using PBE functional Ultrasoft pseudopotentials Plane-wave basis set (30 Ry energy cutoff, 180 Ry charge density cutoff) Monkhorst-pack mesh for Brillouin zone sampling Structural optimization via Hellman-Feynman forces	Band alignment and offsets were calculated using supercell periodic slab models BaTiO3/Cu2O interface shows a staggered (Type-II) band alignment, which favors charge separation and enhances photoelectrochemical activity Band offset values were obtained by considering valence band (Ev) and conduction band (Ec) discontinuities Effective mass of electrons and holes was calculated, revealing that Cu2O has a lower electron effective mass, indicating higher carrier mobility The interface has a built-in dipole due to electronic charge transfer, influencing potential shifts across the heterojunction
[169] BaTiO3 (BTO) (001) surfaces, including perfect and oxygen-deficient (TiO2-terminated) surfaces	DFT with DFT+U using the VASP	PBE+U(Ti,O) approach improves the accuracy of band gap calculations and bond energy predictions compared to standard PBE and PBE+U(Ti). Oxygen vacancies (Ovac) introduce in-gap states with Ti-3d character, positioned ~1.0 eV above the valence band maximum (VBM) and ~0.8 eV below the conduction band minimum (CBM). The stability of BaO- and TiO2-terminated surfaces depends on temperature: BaO is more stable at 0K, but TiO2 dominates at high temperatures (>1000K). Formation of Ovac is energetically more favorable on TiO2-terminated surfaces than on BaO-terminated surfaces. Adsorption of oxygenated species (O*, HO*, HOO*) occurs preferentially on Ti5c sites, with binding energies increasing from the perfect surface to the reduced surface (cBTO-TiO2 → cBTO-TiO2−x). Adsorption of O* exhibits two states: radical adsorbate and surface hole (h+), with a transition state energy barrier of ~0.3 eV. The reaction step from radical O* to surface hole (h+) involves electron transfer from a surface oxygen atom connected to the Ti adsorption site.

 doi:10.20944/preprints202506.0553.v1

Rizwan et al. conducted a first-principles investigation of $BaTiO_3$ and La-doped $BaTiO_3$ using the CASTEP program based on Density Functional Theory (DFT) with the GGA-PBE functional [141]. Their study examined structural, electronic, and optical properties before and after doping. The optimized lattice parameter for pure $BaTiO_3$ was 4.034 Å, closely matching experimental values, while La doping reduced it to 3.971 Å. Band structure analysis revealed that pure $BaTiO_3$ exhibited an indirect band gap (1.723 eV), which transformed into a direct band gap (1.569 eV) upon La doping, enhancing conductivity by facilitating electron-hole recombination. The La-5d states played a crucial role in modifying the conduction band. Optical properties, including refractive index (2.598 for pure, 2.482 for doped) and absorption, were significantly affected by doping. The results demonstrated strong agreement with previous theoretical and experimental findings, validating the computational approach used in their study.

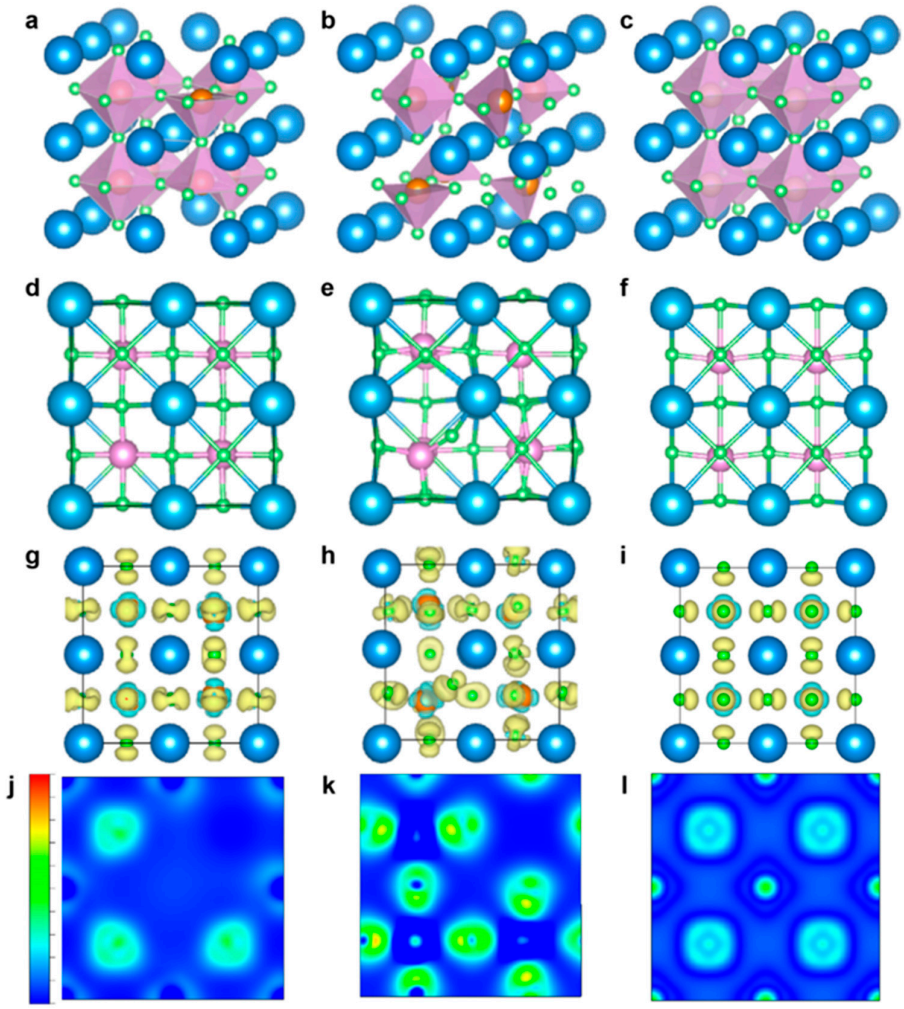

Figure 5. $BaTiO_3$ lattice structure representations: (a) Ba vacancy, (b) Ti vacancy, and (c) ideal tetragonal $BaTiO_3$. (d) Ba and (e) Ti vacancies. (f) Front view of the tetragonal $BaTiO_3$ model; front view of lattice structure simulation results. Charge density difference (CDD) for (g) Ba vacancy and (h) Ti vacancy. (i) Ideal tetragonal $BaTiO_3$ model viewed along the [001] zone axis. CDD contour maps for (j) Ba vacancy and (k) Ti vacancy. (l) Ideal tetragonal $BaTiO_3$ model. The intercepts are shown at 0d, 0.25d, and 0.5d. Ba is represented in light blue, Ti in light orange, and O in light green.

Xu et al. investigated the impact of Ba/Ti ratio on the tetragonality of $BaTiO_3$ powder, challenging the conventional view that attributes tetragonality solely to grain size [142]. Their study demonstrated that as the Ba/Ti ratio increased from 0.990 to 1.010, the particle size remained stable

 doi:10.20944/preprints202506.0553.v1

at approximately 200 nm. Tetragonality initially rose from 1.006 to a peak of 1.0092 at Ba/Ti = 1.000 before declining to 1.005. Using density functional theory (DFT), they analyzed electron density and lattice distortion, revealing that both Ba and Ti vacancies influence lattice deformation, with Ti vacancies causing more significant lattice expansion and reduced tetragonality. Their findings were supported by calculated charge density distributions, which showed that Ti vacancies increased charge uniformity. Using this optimized $BaTiO_3$ powder, they fabricated high-density ceramics and multilayer ceramic capacitors (MLCCs) with X7R temperature stability, highlighting the potential of Ba/Ti ratio control in developing advanced dielectric materials.

Xie et al. investigated the enhancement of photocatalytic hydrogen production through Mo doping in $BaTiO_3$ (BTO) [143]. To improve light absorption, they synthesized Mo-doped BTO via a solid-state reaction and modified the samples with 0.4 wt% Pt using a photoreduction method. Their findings revealed that Mo doping significantly narrows the bandgap, shifting the absorption edge into the visible-light region. Compared to pure BTO, which has a hydrogen evolution rate of 35 mmol g^{-1} h^{-1}, Mo-doped BTO (2 at%) achieved 63 mmol g^{-1} h^{-1}, nearly twice the efficiency. First-principles density functional theory (DFT) calculations demonstrated that the hybridization between Ti 3d and Mo 3d orbitals led to a downward shift in the conduction band minimum, explaining the improved photocatalytic performance. Their study highlights how bandgap engineering via dopant selection enhances light absorption and provides valuable insights for designing high-performance metal-oxide photocatalysts for solar-driven hydrogen production.

Usman et al. conducted a theoretical investigation into the structural, electronic, and optical properties of pure and Cs-doped $BaTiO_3$ using the CASTEP code [144]. Their study employed the plane-wave pseudopotential method with the Perdew-Burke-Ernzerhof (PBE) exchange-correlation functional and the DFT+U approach to enhance electronic property accuracy. The calculated lattice parameter for pure $BaTiO_3$ was 4.034 Å, with an indirect band gap of 2.513 eV, aligning well with prior research. Upon Cs doping (0.13%, 0.26%, and 0.39%), the band gap transitioned to a direct type, with values of 1.858 eV, 2.103 eV, and 1.882 eV, respectively. Notably, 0.13% Cs-doped $BaTiO_3$ exhibited the highest absorption edge in the visible spectrum and the lowest energy loss, making it a promising candidate for photocatalytic water splitting. The introduction of Cs-3p states into the valence band enhanced photocatalytic activity, particularly in the visible range, improving $BaTiO_3$'s potential for energy applications.

Chun et al. investigated the surface termination of single-crystal $BaTiO_3$(111) using a combination of Density Functional Theory (DFT) and X-ray Photoelectron Spectroscopy (XPS) [145]. Their study focused on the stability of stoichiometric (BaO_3 and Ti) and non-stoichiometric (BaO_2, O, BaO, O_2, Ba, and O_3) terminations. DFT+U calculations revealed that BaO_2 and O terminations exhibit the lowest cleavage and surface energies, making them the most stable under different conditions. The presence of Ti^{3+} states and oxygen defects was confirmed through XPS analysis of the O 1s and Ti 2p regions. Further DFT calculations of O 1s chemical shifts indicated that OH* species preferentially adsorb on O-terminated surfaces, closely matching experimental XPS data. Their findings suggest that $BaTiO_3$(111) favors an OH*-covered O termination, with surface defects playing a crucial role in stabilizing the polar surface.

Dahbi et al. investigated the thermodynamic stability, electronic structures, and optical properties of pure and compressed $BaTiO_3$ doped with varying concentrations of oxygen group elements (S, Se, and Te) using Density Functional Theory [146]. Their findings revealed that substituting oxygen atoms with chalcogen elements significantly reduced the forbidden band gap from 3.010 eV (for compressed $BaTiO_3$) to 0.000 eV (for Te-doped $BaTiO_3$), highlighting the crucial role of chalcogen impurities in modifying the electronic properties of $BaTiO_3$. Additionally, applying a 2.3% compressive strain, with or without chalcogen doping, transformed $BaTiO_3$ from an indirect to a direct semiconductor. The calculated formation energy confirmed the thermodynamic stability of all studied compounds. Furthermore, doping altered the absorption behavior of $BaTiO_3$, making it more suitable for optoelectronic applications due to the introduction of additional charge carriers

 doi:10.20944/preprints202506.0553.v1

into the system. These findings provide valuable insights into the potential applications of doped $BaTiO_3$ in electronic and optical devices.

Dahbi et al. investigated the impact of compressive strain on the electronic, optical, and thermoelectric properties of cubic and tetragonal phases of BTO perovskite-type crystals using Density Functional Theory (DFT) [147]. Their study revealed that applying a compressive strain of 2.3% or higher transforms BTO into a semiconductor with a direct bandgap, eliminating additional interactions in the conduction band—an important characteristic for photovoltaic applications. Additionally, the bandgap width increased with strain, highlighting the piezoelectric nature of BTO. The optical analysis indicated that both pure and strained BTO exhibit strong optical properties across the visible and UV spectra. Furthermore, compressive strain enhanced hole mobility, leading to improved thermal and electrical conductivity. A shift in absorption coefficient and optical conductivity peaks to higher UV energies further supported the piezoelectric behavior of BTO. These findings underscore the potential of strained BTO in electronic and energy-related applications.

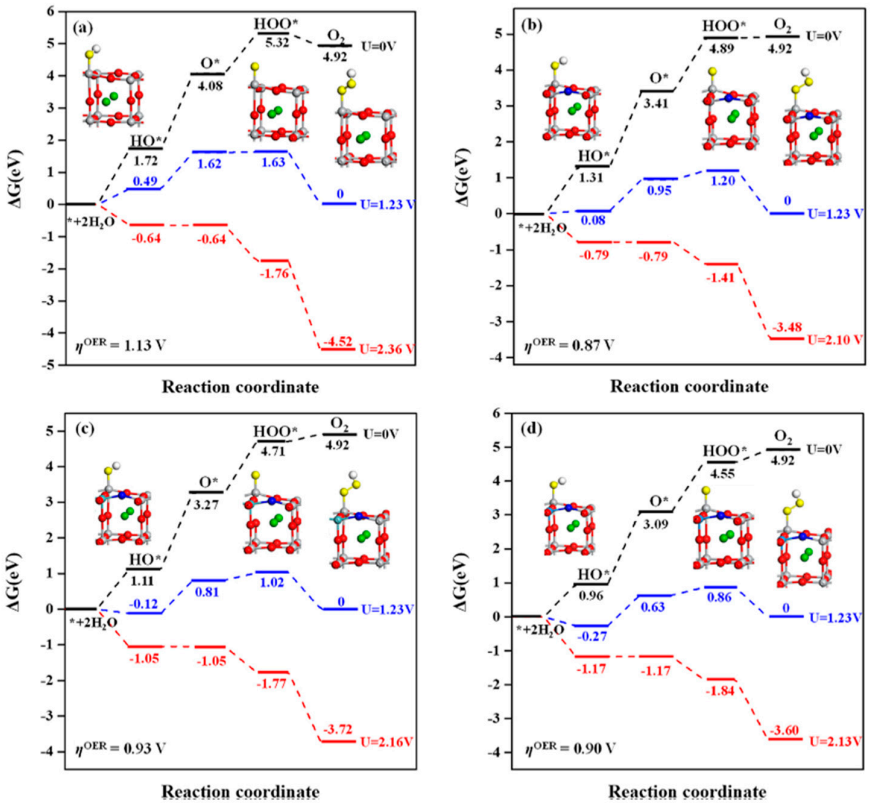

Figure 6. Free energy diagrams for the oxygen evolution reaction (OER) at the Ti site on $BaTiO_3$ (001) surfaces at pH = 0 and T = 298 K under different applied potentials: (a) pure, (b) (V + N)-codoped, (c) (Nb + N)-codoped, and (d) (Ta + N)-codoped systems.Reprinted with permission from [148]. Copyright 2022, for Elsevier [148].

Fo et al. conducted a density functional theory (DFT) study to examine the effects of metal-nonmetal co-doping on the stability, electronic properties, and photocatalytic activity of tetragonal $BaTiO_3$ (001) surfaces [148]. Their findings indicate that co-doped systems (M = V, Nb, Ta, Mo, W; X = N, C) are energetically stable, favoring formation in O-rich conditions. Most co-doped surfaces exhibit significantly reduced bandgaps, enhancing visible-light absorption. Additionally, co-doping improves water affinity and modifies active sites for the hydrogen evolution reaction (HER) and oxygen evolution reaction (OER), with the O site and Ti site (adjacent to the metal dopant) acting as active centers, respectively. Notably, passivated co-doping lowers the HER free energy barrier and reduces the OER overpotential compared to pristine $BaTiO_3$. Among the studied systems, Ta+N,

 doi:10.20944/preprints202506.0553.v1

W+N, Mo+N, Mo+C, Mo+2N, and W+2N co-doped $BaTiO_3$ are highlighted as promising photocatalysts for overall water splitting.

Chakraborty et al. investigated the structural, electronic, and optical properties of $BaTiO_3$ using density functional theory (DFT), highlighting its potential for photocatalytic applications, including water splitting and pollutant degradation [149]. Their study employed the hybrid HSE06 functional, yielding bandgap values of 3.254, 3.894, 3.694, 3.519, and 3.388 eV for cubic, rhombohedral, orthorhombic, tetragonal, and hexagonal $BaTiO_3$ polymorphs, respectively. Notably, this was the first DFT-based study to closely match experimental bandgap values. Electronic band structure analysis revealed that all polymorphs exhibit semiconducting behavior, with indirect bandgaps except for the hexagonal phase, which has a direct bandgap. The density of states analysis indicated significant hybridization between O-2p and Ti-3d states. Optical studies confirmed strong absorption, low reflectivity, and optical anisotropy in the orthorhombic and tetragonal phases, making $BaTiO_3$ suitable for UV-based optical devices, waveguides, and dielectric applications. The findings suggest $BaTiO_3$'s strong redox potential enhances its photocatalytic efficiency.

Bhat et al. successfully synthesized a porous graphene-$BaTiO_3$ (PGBT) nanocomposite using a simple one-pot solvothermal method and investigated its photocatalytic efficiency in degrading methylene blue (MB) dye under visible light [150]. The combined experimental and theoretical analysis demonstrated enhanced photocatalytic performance, attributed to the formation of Ba–C bonds, which facilitated charge carrier transport and suppressed recombination. Additionally, the reduced band gap due to hybridized states extended light absorption into the visible range, while the high surface area provided more active sites for MB adsorption. The PGBT composite exhibited a threefold increase in photodegradation efficiency compared to pure $BaTiO_3$, achieving 98.6% degradation within 80 minutes. Furthermore, it showed excellent cyclic stability, highlighting its potential as a durable photocatalyst for environmental remediation. This study serves as a valuable reference for designing PG-based nanocomposites, leveraging solar energy for sustainable pollutant degradation.

Bashir et al. conducted a theoretical investigation of gallium-modified barium titanate (Ga-BTO) perovskite ceramics ($Ba_{1-x}Ga_xTiO_3$, x = 50%) using density functional theory-based full potential linear augmented plane wave (FP-LAPW) calculations [151]. Their study explored the optoelectronic, elastic, and mechanical properties of both pure and Ga-doped $BaTiO_3$. The results revealed that Ga substitution altered the electronic structure, reducing the bandgap to 1.84 eV and inducing half-metallic behavior with 100% spin polarization. Optical analysis indicated enhanced absorption in the ultraviolet region, a lower reflectivity, and a static refractive index of 12.2. The modified BTO exhibited higher ductility, anisotropy, and bulk modulus (169.96 GPa) compared to the pure form. Additionally, prominent peaks in optical conductivity at 4.2 and 5.8 eV suggested potential applications in optoelectronics and spintronics. These findings highlight Ga-BTO as a promising material for infrared detectors and antireflective coatings.

Wang et al. developed a flower-like core–shell heterostructured oxygen evolution reaction electrocatalyst by integrating tetragonal BaTiO3 nanoparticles (t-BTO NPs) with NiFe-layered double hydroxide (NiFe-LDH) nanoarrays [152]. The study explored how the self-polarization effect of t-BTO influenced the OER performance of NiFe-LDH. In alkaline media (1.0 M KOH), the t-BTO@NiFe-LDH heterojunction exhibited a remarkably low overpotential of 186 mV at 10 mA/cm² and a Tafel slope of 38.3 mV dec^{-1}, outperforming its individual components. Density functional theory (DFT) calculations demonstrated that electronic modulation between t-BTO and NiFe-LDH reduced the bandgap, enhanced conductivity, and optimized the adsorption of oxygen-containing intermediates. Projected density of states (PDOS) analysis confirmed that t-BTO facilitated rapid electron transfer through self-polarization. The synergistic effects of these heterostructures resulted in superior electrocatalytic activity, offering insights into the rational design of efficient, noble-metal-free OER electrocatalysts.

Chen et al. developed an amorphous PtOx-supported BaTiO3 catalyst (BTPOv-0.09) with oxygen vacancies (Figure 7), designed for efficient hydrogen (H_2) production from wastewater while

 doi:10.20944/preprints202506.0553.v1

simultaneously degrading organic pollutants [153]. The catalyst features Pt-O-Ti^{3+} charge separation sites, enhancing photocatalytic efficiency. BTPOv-0.09 achieved a remarkable H_2 generation rate of 1891 μmol·g^{-1}·h^{-1} and exhibited a degradation rate constant (k) of 0.0485 min^{-1} for pefloxacin (PFX), significantly outperforming pristine BaTiO3. The introduction of PtOx facilitated oxygen vacancy formation, improving charge transfer and catalytic activity. X-ray absorption spectroscopy and HAADF-STEM analysis confirmed the presence of PtOx. The Pt sites optimized H* adsorption and H_2 desorption, while Ti^{3+} sites enhanced PFX adsorption. As a result, BTPOv-0.09 demonstrated superior performance, achieving 98.1% PFX removal within 90 minutes. This work highlights an effective strategy for developing bifunctional photocatalysts by engineering multiple active sites on a single catalyst for simultaneous redox reactions.

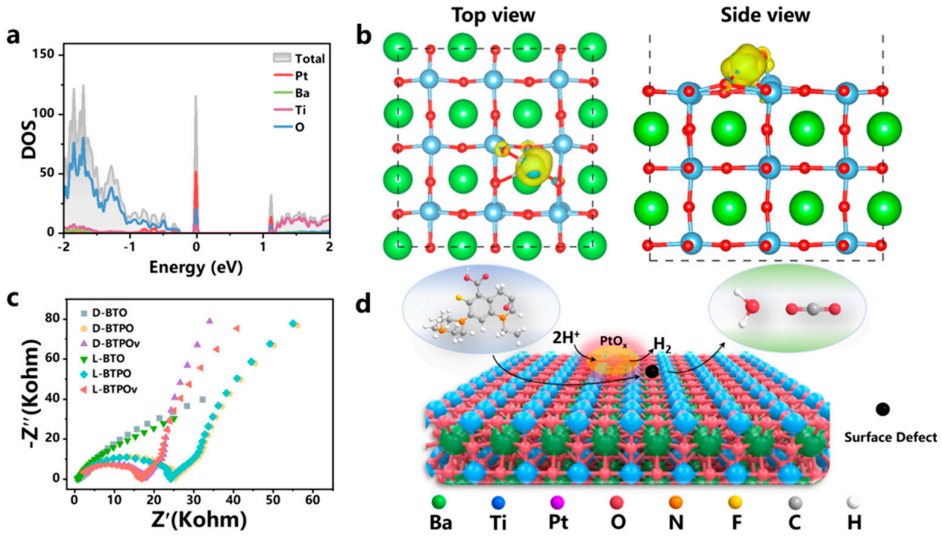

Figure 7. Interface reaction mechanism: (a) DOS configuration file for BTPOv-0.09, (b) top and side views of charge distribution in BTPOv-0.09, (c) EIS Nyquist plots of BTO, BTPO-0.09, and BTPOv-0.09 under dark and light conditions, and (d) reaction mechanism diagram of BTPOv-0.09.Reprinted with permission from [153]. Copyright 2024, for Elsevier [153].

Guo et al. explored the synergistic effect between piezoelectricity and photocatalysis to enhance hydrogen production via water splitting [154]. By combining experimental and theoretical analyses, they demonstrated that the inherent piezoelectric field in BaTiO3 can reduce the bandgap of SrTiO3/BaTiO3 heterojunction nanofibers, facilitating electron transfer through the Z-scheme mechanism. The incorporation of piezoelectric BaTiO3 significantly boosted the hydrogen evolution rate of SrTiO3/BaTiO3 nanofibers to 1950.2 μmol·g^{-1}·h^{-1}, surpassing pure SrTiO3 and BaTiO3 by factors of 2.4 and 4.1, respectively. This rate also exceeded previously reported perovskite-based piezo-photocatalysts. Fabricated via electrospinning followed by thermal treatment, these nanofibers exhibited enhanced charge separation due to the piezoelectric field generated under ultrasonic vibrations. Their findings highlight the crucial role of piezoelectric-assisted photocatalysis in improving energy band alignment and efficiency, paving the way for advanced photocatalysts that address energy and environmental challenges in sustainable hydrogen production.

Zulfiqar et al. investigated the potential of chalcogen doping (X = S, Se, Te) in $BaTiO_3$ for visible-light-driven photocatalysis in hydrogen production [155]. Using first-principles density functional theory (DFT) calculations with the SCAN meta-GGA functional, they assessed the structural, thermodynamic, electronic, and optical properties of X-doped $BaTiO_3$. Their results indicated that incorporating a chalcogen atom at an oxygen site in $BaTiO_3$ is thermodynamically challenging due to significant differences in atomic radii and electronegativities. To enhance the synthesis feasibility, they proposed Zr codoping at Ti-sites, which improved thermodynamic stability while maintaining

 doi:10.20944/preprints202506.0553.v1

band gap reduction. Electronic structure calculations using the TB-mBJ functional showed that Zr+Xcodoping converted $BaTiO_3$ into a direct band gap material with band edge positions favorable for overall water splitting. This study highlights the potential of Zr+Xcodoped$BaTiO_3$ as an efficient photocatalyst for hydrogen evolution under both oxygen-rich and oxygen-poor conditions.

Kovač et al. investigated the role of transport layers in perovskite solar cells, focusing on their charge carrier extraction and transfer mechanisms [156]. Using ab initio calculations, they examined the interface properties of metal oxide/$BaTiO_3$ heterostructures, identifying key competing factors influencing charge dynamics. Their findings highlight the impact of band gap character on charge carrier mobility, where a direct band gap reduces electron-hole lifetime and diffusion length. Additionally, they explored the influence of electrostatic potential variations, which enhance charge transfer rates but are counteracted by unfavorable conduction band offsets. The study emphasizes the importance of interlayer morphology over intrinsic material properties, suggesting that optimizing atomic plane distances and atomic number distributions can improve charge transport efficiency. They further propose that ultra-thin buffer layers may enable charge tunneling, similar to effects observed in CIGS solar cells with CdS layers. These insights provide guidelines for designing enhanced buffer layers in perovskite solar cells.

Kaptagay*et al.* investigated the oxygen evolution reaction (OER) on a Rh-doped $BaTiO_3$ (001) surface using DFT calculations [157]. Their study assessed the Gibbs free energy changes for each reaction step and calculated the overpotential while considering solvation effects. The findings revealed that Rh doping significantly reduces the overpotential compared to the undoped $BaTiO_3$ surface, which exhibits low OER efficiency. This improvement is attributed to the oxidation state transition of Rh from 3+ to 4+ during water splitting, which enhances the charge transfer from surface oxygen ions. As a result, the binding energy between surface ions and adsorbates increases, weakening the adsorbate-adsorbate interactions and leading to a lower overpotential. The reduced overpotential on the Rh-modified TiO_2 surface confirms its enhanced catalytic activity in electrochemical water oxidation, aligning well with experimental results and previous studies. These insights highlight Rh doping as a promising strategy for improving OER efficiency.

Opoku et al. investigated the electronic structure, charge transfer, and photocatalytic properties of cubic $LaAlO_3$(001) modified with cubic $BaTiO_3$(001), (011), and (111) surfaces [158]. Their study aimed to understand how $LaAlO_3$ can be activated under light irradiation through the incorporation of different $BaTiO_3$ surfaces. The heterostructures demonstrated a reduced bandgap energy, enhancing visible light absorption. Additionally, $BaTiO_3$/$LaAlO_3$(001) heterostructures exhibited a staggered type-II band alignment, which facilitated charge carrier separation and minimized recombination. The $BaTiO_3$(001) surface, in particular, enhanced photocatalytic activity due to its complex surface structure and active barium adsorption sites. $BaTiO_3$ acted as a sensitizer, improving overall photoactivity. Their findings provide valuable insights into the preferential exposure of photocatalytic active surfaces, aiding in the design of advanced heterostructures for photocatalytic applications and offering a deeper understanding of photocatalytic mechanisms.

Abbasi et al. investigated the impact of ferroelectric polarization on the electronic structure and electrocatalytic activity of $BaTiO_3$ thin films, particularly in the hydrogen evolution reaction (HER) [159]. Unlike previous studies focused on nanoparticle systems with complex interfaces, they used molecular beam epitaxy (MBE) to grow epitaxial $BaTiO_3$ films with atomically sharp interfaces. Their surface spectroscopy and ab initio DFT+U calculations revealed that upward polarization decreases the work function and lowers the HER barrier, correlating with enhanced experimental activity. The study demonstrated that modulating polarization can dynamically switch between distinct electrocatalytic surfaces, altering charge transfer resistance and exchange current density. The findings highlight how ferroelectric layers can be used to control intermediate binding energies in electrochemical reactions, offering new avenues for nanoscale catalyst design by leveraging polarization-dependent surface properties beyond conventional catalytic descriptors.

Gunawan et al. investigated the role of ferroelectric polarization in enhancing photoelectrochemical (PEC) performance, addressing challenges related to charge recombination and

 doi:10.20944/preprints202506.0553.v1

sluggish charge transfer kinetics [160]. They designed a heterostructure composed of multiferroic bismuth ferrite (BFO) and photoactive bismuth vanadate (BVO) in a neutral pH electrolyte, demonstrating significant photocurrent improvements. Notably, both polarization states contributed to enhancement: the down-poled BFO/BVO exhibited a 136% increase, while the up-poled configuration showed a 70% improvement at 1.23 V_RHE, surpassing previous reports. Extensive PEC analysis, surface characterization, and density functional theory (DFT) calculations revealed that the improvements were driven by band energy gradient modulation, band bending, and altered BFO/adsorbate interactions. The sol–gel synthesis method used is scalable and employs environmentally friendly materials, making this approach promising for next-generation dynamic photoelectrodes. Their findings advance the field of ferroelectric-based PEC systems by enabling tunable charge dynamics and overcoming limitations of conventional semiconductor photoelectrodes.

Goumri-Said et al. conducted a comprehensive study on the electronic properties and optical absorption behavior of anion-anion co-doped BaTiO3 to design efficient photocatalysts for water redox reactions [161]. Using first-principles hybrid density functional theory (DFT) calculations with the HSE06 functional, they analyzed the impact of double-hole doping on band structure modifications. Their findings revealed that the formation energy of mono- and co-doped configurations increased as the oxygen chemical potential decreased, with N–N co-doped BaTiO3 exhibiting the most favorable formation energy under O-poor conditions. All co-doping configurations resulted in band gap reduction, enhancing visible light absorption and aligning band edge positions with water oxidation-reduction potentials. This study highlights the effectiveness of anionic co-doping in tuning wide-bandgap semiconductors, demonstrating that such modifications can produce highly efficient photocatalysts for solar-driven water splitting.

Chandrappa*et al.* explored strategies to modify the electronic and optical properties of $BaTiO_3$ (BTO) by introducing Ir doping at Ti sites [162]. While pristine BTO typically exhibits strong n-type behavior and ultraviolet absorption ($\lambda \leq 390$ nm), their study demonstrated a successful transition to p-type semiconducting behavior with extended visible-light absorption ($\lambda \leq 600$ nm). Through a combination of advanced spectroscopy, microscopy, and computational electronic structure analysis, they elucidated the underlying mechanisms governing this transition. The redshift in optical absorption was attributed to the formation of Ir^{3+}/Ir^{4+} in-gap energy levels within the bandgap, facilitating optical transitions. Furthermore, the observed decrease in Ti^{3+} donor levels and correlated oxygen vacancies played a crucial role in enabling the p-type behavior. These findings highlight the potential of Ir-doped BTO as a promising visible-light-absorbing semiconductor with significant applications in optoelectronics and solar fuel generation.

Bhat et al. investigated the potential of environmentally friendly BaTiO3 as a photocatalyst, despite its initially wide band gap, which limits efficiency [163]. They explored Rh doping to reduce the band gap but avoided the formation of mid-gap recombination centers that typically hinder photocatalytic performance. Using first-principles DFT calculations, they determined that Rh occupying both Ba and Ti sites simultaneously would introduce detrimental acceptor states. To address this, they employed a hydrothermal synthesis method to direct Rh towards Ba sites, leading to donor Rh^{3+} states that lowered the band gap while maintaining high photocatalytic activity. Their experimental results confirmed an efficient 96% degradation of methylene blue dye within 120 minutes for a 0.5 Rh-doped sample. This study demonstrated a viable strategy to enhance BaTiO3's photocatalytic efficiency and suggested that similar methods could be applied to other perovskite oxides for improved dye degradation.

Qiu et al. investigated the impact of switchable polarization in ferroelectric catalysts on the hydrogen evolution reaction (HER), aiming to overcome the Sabatier limit faced by traditional catalysts [164]. Using $BaTiO_3$ (BTO) as a model system, they demonstrated that HER activity is tunable by controlling polarization states. First-principles calculations revealed that in-plane polarized BTO enhances HER performance compared to out-of-plane polarization, due to surface dipole–dipole interactions. Surface rumpling, influenced by polarization states, significantly affects

 doi:10.20944/preprints202506.0553.v1

surface oxygen reactivity, with an optimal 2p band center correlating to improved HER activity. The study also established a link between hydrogen adsorption energy and polarization effects. Furthermore, a HER catalytic cycle leveraging switchable polarization states was proposed, showing potential for enhanced catalytic efficiency. Their findings highlight the role of ferroelectric polarization control in designing high-performance electrocatalysts, providing insights into functional ferroelectric catalysis beyond HER applications.

Wang et al. investigated the impact of co-doping rare earth elements on the electronic and photocatalytic properties of BaTiO3 using first-principles calculations [165]. They examined BaTiO3 supercell structures with La concentrations of 12.5% and 25%, focusing on doping at both Ba and Ti sites. Their analysis of band structure, density of states, and charge density difference revealed that co-doping 25% La at the Ti site significantly enhanced visible light absorption and water-splitting performance. The introduction of La created intermediate energy levels within the bandgap, reducing the energy required for electronic transitions. Further, La-N co-doping at the Ti site effectively modified the band structure, improving photocatalytic efficiency. Optical property calculations confirmed an extended absorption edge, enhancing BaTiO3's visible light response. Their findings highlight La co-doping as a promising strategy for optimizing BaTiO3's electronic structure and photocatalytic activity, making it a viable material for energy-related applications.

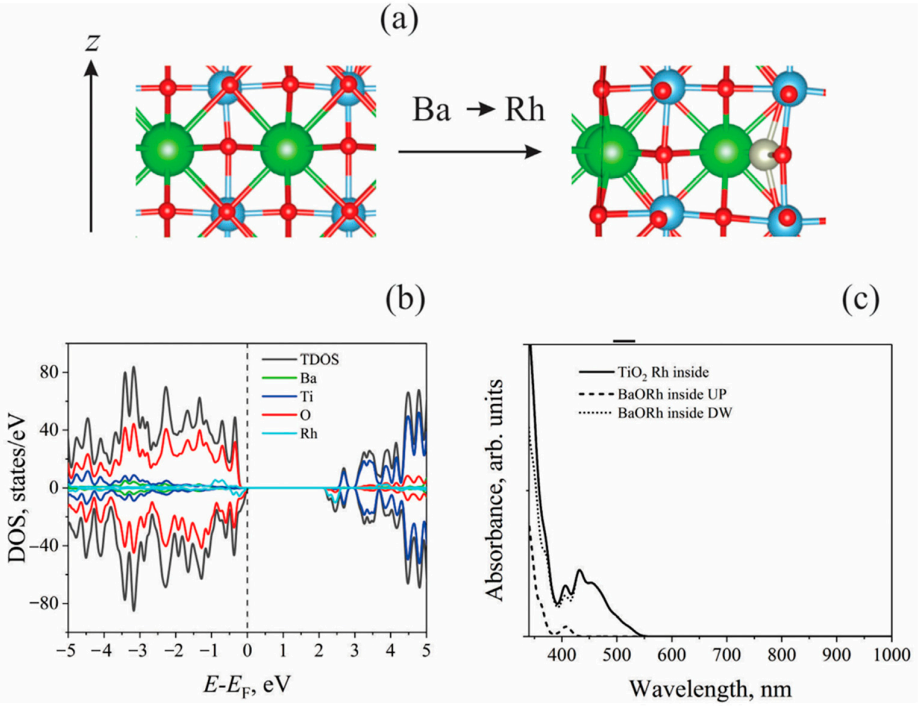

Figure 8. (a) Ion arrangement changes in the slab after Ba substitution with Rh, (b) electronic DOS of the relaxed slab, and (c) optical absorption spectrum of the investigated model. Dashed and dotted lines indicate optical absorption for spin-up and spin-down states, while the solid line represents total absorption. Reprinted with permission from [57]. Copyright 2024, for MDPI [57].

Inerbaev et al. explored the potential of modified barium titanate ($BaTiO_3$), a cost-effective perovskite oxide, as an efficient water oxidation electrocatalyst using first-principles calculations [57,135]. Their study demonstrated that Rh doping enhances $BaTiO_3$'s light absorption capabilities while reducing the overpotential required for water oxidation. The TiO_2-terminated $BaTiO_3$ (001) surface was identified as particularly promising for catalytic applications. Rh doping expanded the material's absorption spectrum to cover the entire visible range, with the aqueous environment playing a crucial role in modulating its solar radiation absorption. Upon Ti→Rh substitution,

 doi:10.20944/preprints202506.0553.v1

rhodium ions partially acquired electron density from surrounding oxygen atoms, stabilizing an intermediate oxidation state (3+ to 4+) during water oxidation. This interaction influenced the adsorption energies of reaction intermediates, effectively lowering the overpotential. The study concluded that Rh-modified $BaTiO_3$ surfaces exhibit significant potential as photoanodes in photoelectrochemical systems for water oxidation.Inerbaev et al. investigated also the optical properties of tetragonal $BaTiO_3$ using density functional theory, incorporating both static lattice calculations and ab initio molecular dynamics [135]. Their study, which applied GGA + U and hybrid functionals, revealed that atomic motion significantly lowers the optical absorption threshold. This reduction occurs due to thermal fluctuations enabling previously forbidden electronic transitions and shifting the energy levels of optical absorption, providing insights into the photoluminescence behavior of $BaTiO_3$.

Saadon et al. investigated the structural, electronic, and optical properties of platinum (Pt)-doped cubic BaTiO3 perovskite using density functional theory (DFT) calculations. By employing the CASTEP code with the generalized gradient approximation (GGA) and PW91 functional, they examined the effects of substituting 0.125 Pt at Ba and Ti sites. Their findings showed that Pt doping reduced the band gap to 1.78 eV and 2.06 eV for Ba and Ti substitution, respectively, and introduced Pt-5d states in the conduction band, significantly influencing electronic properties. Additionally, the optical absorption spectrum exhibited a red shift, extending into the visible range, making Pt-BaTiO3 a promising material for optoelectronic applications. The negative formation energy confirmed the thermodynamic stability of the doped system. Mulliken charge analysis further revealed a shift from ionic to covalent bonding in Ba–Pt and Ti–Pt interactions. Future studies may explore the material's potential in photocatalysis and environmental applications [166].

Sharma et al. synthesized nanostructured BaTiO3/Cu2O heterojunction electrodes with varying Cu2O film thickness using spray deposition onto spin-coated BaTiO3 thin films [167]. For the first time, first-principles density functional theory (DFT) calculations were performed to determine band offsets and effective masses of charge carriers for bulk BaTiO3 and Cu2O. The study revealed enhanced separation of photogenerated charge carriers at the BaTiO3/Cu2O interface. Experimental photoelectrochemical (PEC) analysis confirmed these findings, showing a maximum photocurrent density of 1.44 mA/cm² at 0.95 V/SCE for a 442 nm thick heterojunction electrode. This structure exhibited superior charge transfer, reduced resistance, and improved light absorption compared to individual BaTiO3 or Cu2O electrodes. The study demonstrated that BaTiO3/Cu2O heterojunctions improve water-splitting efficiency in PEC cells, achieving a peak conversion efficiency of 0.66%, outperforming FeTiO2/Zn-Fe2O3 heterojunctions. Theoretical results aligned well with experimental data, providing insights into charge separation mechanisms.

Tyminska et al. investigated the impact of oxygen vacancies (Ovac) on the oxygen evolution reaction (OER) at the TiO2-terminated (001) surface of cubic BaTiO3 (cBTO-TiO2) using spin-polarized DFT+U calculations and the standard four-step proton-coupled electron transfer (PCET) mechanism [169]. Their study revealed that excess electrons from Ovac contribute to charge transfer (CT) with intermediate adsorbates (HO*, O*, and HOO*) or generate surface oxygen hole states. This CT enhances the binding energies of these species in proportion to their electronegativity. Notably, HO* and O* are stabilized more strongly than HOO*, leading to increased OER overpotential (ηOER) on the oxygen-deficient surface. This contradicts experimental findings that indicate enhanced efficiency for oxygen-deficient BTO, suggesting that a different mechanism or surface structure may be responsible under experimental conditions. Additionally, they identified novel HO* and O* adsorption structures that induce surface oxidation, attributed to the low work function of Ti–O–Ti moieties.

 doi:10.20944/preprints202506.0553.v1

2.2. Ab initio MD Simulations

Atomistic simulations play a crucial role in understanding the fundamental mechanisms governing photocatalytic activity in $BaTiO_3$-based systems [59]. Among these methods, ab initio MD simulation is widely employed to capture the electronic structure and dynamic behavior of catalytic interfaces at finite temperatures. However, ab initio MD simulations are computationally expensive, limiting their application to short timescales [170–175]. To overcome this limitation, machine learning potentials (MLP) trained on DFT data have been developed, offering an efficient alternative for extended simulations while retaining DFT-level accuracy [176–184].

This study employs machine learning potentials (MLP) to investigate the oxygen evolution reaction through metadynamics simulations. Figure 7 outlines the MLP training process, which involves constructing a dataset that captures the configurational space of oxygen evolution reaction over $BaTiO_3$ and Ni@$BaTiO_3$ slabs [59]. Additionally, single-point DFT calculations can be applied to selected structures, improving efficiency through parallelization, unlike the inherently sequential nature of MD.

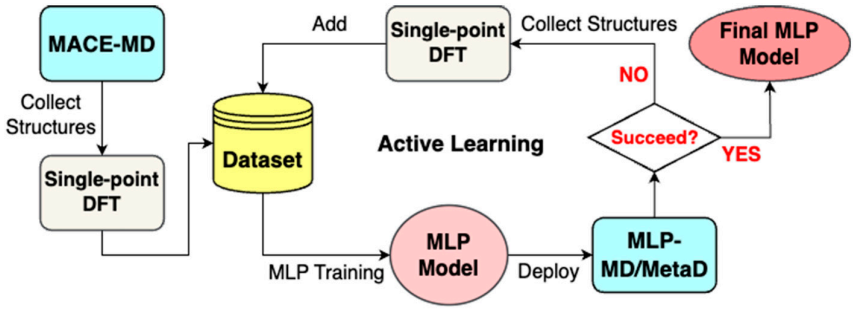

Figure 7. Overview of the MLP training workflow for MD simulations using DFT data.Reprinted with permission from [59]. Copyright 2024, for the arXiv [59].

The stepwise mechanism of oxygen evolution reaction mechanism, as depicted in Figure 8, is analyzed using free energy surface calculations.

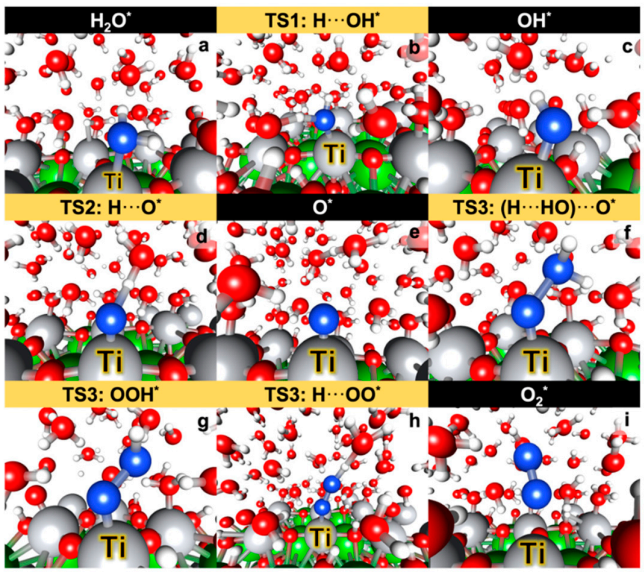

Figure 8. Illustration of the oxygen evolution reaction mechanism observed in the MLP-metadynamics trajectory of the $BaTiO_3$ (4×4)/128H_2O system, with the Ti active site annotated.Reprinted with permission from [59]. Copyright 2024, for the arXiv [59].

 doi:10.20944/preprints202506.0553.v1

The catalytic process was analyzed using ab initio MD simulations with VASP as shown in Figure 9. The newly formed oxygen molecule indicates that oxygen continuously dissolves in water, sustaining OOH generation and continuous H_2O_2 production. Figure 9d,e further reveals the presence of OH radicals, formed either by water oxidation or H_2O_2 decomposition, emphasizing the role of O_2^- radicals in OH radical formation (Table 2).

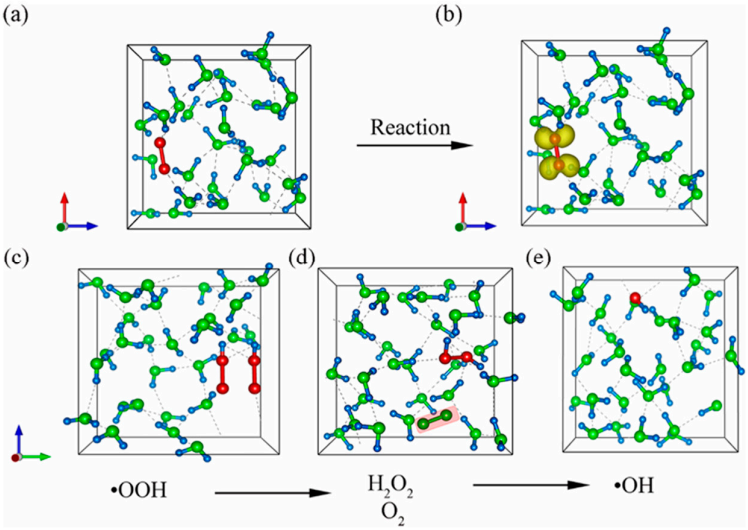

Figure 9. Representations of the ab initio MD simulations, depicting (a) a model with water molecules and a single oxygen molecule before the catalytic reaction and (b) after the reaction. It also includes (c) a model of a single OOH radical before the reaction, (d) the conversion of two OOH radicals into a single H_2O_2 and O_2 molecule, and (e) OH radicals derived from H_2O_2 after the reaction. Reprinted with permission from [185]. Copyright 2024, for the American Chemical Society [185].

Table 2. Recently performed ab initio MD simulation details and main findings.

Designed systems	Methods	Main findings
$BaTiO_3$ surface [59]	- Spin-polarized DFT calculations (VASP) with PAW pseudopotentials and RPBE+D3 functional. - High plane-wave cutoff (520 eV). - Dataset of 16,162 configurations, trained with a 95:5 train-validation split, utilizing a multi-layer perceptron (tanh activation). - MLP models trained using PyTorch with AUC inter-atomic descriptors - MD simulations with MACE-mp-0 model (ASE) MD simulations were conducted at 300 K, 500 K, and 700 K for 50 ps using a pre-trained MACE model. - Production MD simulations: Accelerated with MLP models	- The energy barrier for oxygen desorption is lower than for oxygen evolution reaction, leading to the choice of specific metadynamics parameters (Gaussian height = 0.01 eV, width = 0.05, deposition rate = 6.25 fs). - Water dissociation on the surface forms OH* intermediates with a free energy barrier (ΔG‡ H2O→OH) of 0.06 eV for $BaTiO_3$. - Oxygen evolution reaction steps analyzed using coordination number as collective variables. - Formation of OOH* species occurs when coordination number (Os-Oaw) ≈ 0.3. - Transition from OOH* to O2* is barrierless with rapid proton

 doi:10.20944/preprints202506.0553.v1

	and run for 500 ps at 300 K with a timestep of 0.25 fs. - Metadynamics simulations: Explored oxygen evolution reaction mechanisms using coordination number as collective variables and studied oxygen desorption by tracking Ti-O_2/Ni-O_2 distances. - Well-tempered Metadynamics simulations using PLUMED2-LAMMPS under NVT ensemble	abstraction. - The calculated free energy barrier for the O→O2 transition (ΔG‡ O→O2) is 1.57 eV for $BaTiO_3$ and 1.20 eV for Ni@$BaTiO_3$. - The oxygen desorption step is endothermic, with ΔGO→O2 values of 1.37 eV for $BaTiO_3$ and 0.97 eV for Ni@$BaTiO_3$. - MLP models enable longer simulation times with DFT-level accuracy, improving efficiency compared to ab initio MD.
CTF/$BaTiO_3$ photoanodes [185]	- DFT calculations using VASP 6.3.0 - Perdew-Burke-Ernzerhof (PBE) functional within GGA - Plane wave energy cutoff: 500 eV - k-mesh: 8 × 8 × 8 for bulk and 3 × 2 × 1 for supercell BaTiO3-x - BaTiO3-x slab modeled with (001) surface and (3 × 3 × 1) supercell with 30 Å vacuum - CTF/BaTiO3-x model constructed by depositing CTF on BaTiO3-x slab	- Introduction of CTF reduces the rate-determining step energy barrier from 1.03 eV to 0.84 eV, enhancing oxygen evolution reactionkinetics. - The CTF/$BaTiO_{3-x}$ photoanode achieves a high photocurrent density of 0.83 mA/cm² at 1.23 V (vs. RHE) and a low onset potential of 0.23 V (vs. RHE). - CTF acts as a protective layer, improving stability for real water redox reactions. - Provides a universal strategy for organic/inorganic hybrid photoanodes with high photoconversion efficiency.

Boonpalit *et al.* investigated the oxygen evolution reaction on pristine and Ni-doped$BaTiO_3$ surfaces using metadynamics simulations with machine learning interatomic potentials. Their study aimed to develop cost-effective alternatives to expensive Pt and IrOx/RuOx catalysts for electrocatalytic water splitting. By leveraging artificial neural networks and the MACE-mp-0 model, they created an accurate machine learning potential to simulate oxygen evolution reaction at explicit water interfaces [59]. Their results revealed that Ni-doping enhances $BaTiO_3$'s catalytic activity by lowering the free energy barrier for oxo-oxo bond formation, aligning with experimental findings. However, the study did not account for the lattice oxygen-mediated mechanism, suggesting future work in this area. The database and machine learning potential developed in this study lay a foundation for further investigations into complex catalytic pathways, extending to broader electrochemical reactions at electrode–electrolyte interfaces in explicit solvent environments [59].

Next, Wang et al. investigated the piezo-photocatalytic process by fabricating $Ba_{0.7}Sr_{0.3}TiO_3$ nanorod arrays on fluorine-doped tin oxide-coated glass as recoverable catalysts. Their study demonstrated that the piezoelectric effect significantly enhances photocatalytic efficiency. Under ultrasonic vibrations, the degradation rate constant (k) for rhodamine B using poled $Ba_{0.7}Sr_{0.3}TiO_3$ nanorod reached 0.0447 min^{-1}, which was twice as high as that of the unpoled $Ba_{0.7}Sr_{0.3}TiO_3$ nanorod (0.00183 min^{-1}). This improvement was attributed to the piezoelectric potential generated by poled $Ba_{0.7}Sr_{0.3}TiO_3$ nanorod. Additionally, the $Ba_{0.7}Sr_{0.3}TiO_3$ nanorodarray exhibited a hydrogen production rate of 411.5 μmol g^{-1} h^{-1}. Ab initio MD simulations revealed that hydroxyl radicals (•OH) played a dominant role over superoxide radicals ($•O_2^-$) in the degradation process [185].

 doi:10.20944/preprints202506.0553.v1

2.3. Classical All-Atom MD Simulations

Classical all-atom MD simulations have proven to be an essential tool for understanding the atomic-scale interactions between the $BaTiO_3$ surface and OH^- ions in aqueous environments, particularly under different polarization conditions [186–194]. These simulations provide valuable insights into adsorption behavior, surface charge effects, and polarization-induced modifications that influence $BaTiO_3$'s role in solar water splitting applications. To illustrate this, Figure 10 presents the adsorption of OH^- ions on $BaTiO_3$ surfaces at varying H_2O:OH^- ratios under both unpolarized and positively polarized conditions. Additionally, Table 3 summarizes recent classical all-atom MD studies investigating these interactions, detailing their methodologies and key findings.

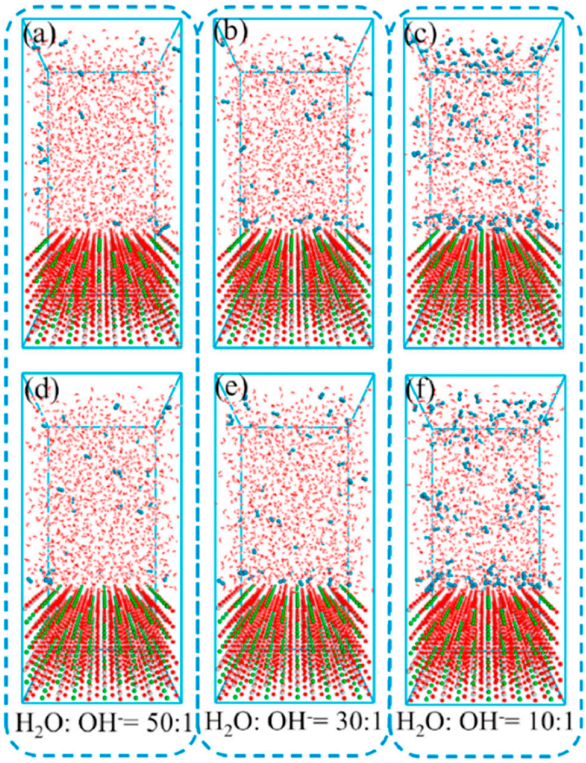

Figure 10. Adsorption of OH^- ions on the $BaTiO_3$ surface at different H_2O:OH^- ratios including (a) unpolarized and (d) positively polarized (0.01 V $Å^{-1}$) $BaTiO_3$ surface at an H_2O:OH^- ratio of 30:1, (b) unpolarized and (e) positively polarized (0.01 V $Å^{-1}$) $BaTiO_3$ surface at an H_2O:OH^- ratio of 10:1, (c) unpolarized and (f) positively polarized (0.01 V $Å^{-1}$) $BaTiO_3$ surface at an H_2O:OH^- ratio of 50:1.Reprinted with permission from [58]. Copyright 2022, for the Elsevier [58].

At lower pH values, the positively polarized sample exhibits the highest Vph, while the negatively polarized sample shows the lowest Vph, indicating that polarization enhances the generation of non-equilibrium carriers (Figure 10). However, at higher pH values, the Vph of both polarized photoanodes decreases compared to the unpolarized sample, aligning with the LSV results. This suggests that at high pH, the presence of $BaTiO_3$ influences the surface behavior differently, impacting the overall performance.

 doi:10.20944/preprints202506.0553.v1

Table 3. Recently performed classical all-atom MD simulation details and main findings.

Designed systems	Methods	Main findings
$BaTiO_3$ surface and its interaction with OH^- ions in an electrolyte [59]	- DFT calculation - CASTEP module in Materials Studio - Classical all-atom MD simulations - Forcite module in Materials Studio - COMPASSIII force field - Electric field of 0.01 eV/Å applied to study positive polarization effects.	- Higher OH^- concentration leads to increased adsorption on the BaTiO surface. - At a 10:1 (H_2O:OH^-) ratio, adsorption is significantly higher compared to a 50:1 ratio. - At a 50:1 (H_2O:OH^-) ratio, polarization significantly impacts OH^- adsorption, but at higher OH^- concentrations, the effect diminishes. - Polarization field enhances photoanode performance in near-neutral conditions by improving surface states and hole collection efficiency.

Chen et al. employed molecular dynamics simulations and density functional theory calculations to investigate the impact of ferroelectric polarization on photoelectrochemicalwater oxidation. Their study demonstrated that the polarization field of $BaTiO_3$ can significantly enhance the photocurrent density of a hybrid α-Fe_2O_3/ $BaTiO_3$photoanode by approximately 30% in near-neutral electrolytes. This improvement is attributed to the polarization-induced enhancement of surface states and donor density within the space charge layer, which facilitates hole collection and improves reaction kinetics. However, computational findings revealed that at high pH values, the adsorption capacity of OH^- ions on polarized and unpolarized $BaTiO_3$ surfaces becomes nearly identical, weakening the effect of the ferroelectric polarization field [58]. Consequently, the polarized field has a minimal influence on photoelectrochemical performance in alkaline conditions. Their work highlights the critical role of electrolyte pH in optimizing ferroelectric materials for photoelectrochemicalapplications, offering new insights into their mechanistic behavior.

While classical all-atom MD simulations have predominantly been used to study $BaTiO_3$ in photoelectrochemical applications, their potential extends to photocatalytic processes as well [195–200]. By investigating ion adsorption, interfacial charge transfer, and surface state modifications, classical all-atom MD simulations can provide deeper mechanistic insights into $BaTiO_3$ based photocatalysts for solar-driven water splitting and related reactions. In conclusion, it is also important to note that calculations of defect-induced Raman modes allow a more in-depth consideration and understanding of the role of surface defects [201–205].

3. Conclusions and Outlook

$BaTiO_3$ has demonstrated significant potential as a photocatalyst for solar water splitting due to its favorable electronic and ferroelectric properties. Atomistic simulations, particularly DFT, ab initio MD, classical all-atom MD, and MLP-based studies, have played a pivotal role in elucidating the fundamental mechanisms governing its photocatalytic activity. DFT calculations have provided insights into band structure modifications, defect engineering, and doping strategies, while ab initio MD and classical all-atom MD simulations have revealed the dynamic interactions of $BaTiO_3$ surfaces with water molecules under realistic conditions. Furthermore, MLP-assisted metadynamics simulations have emerged as a powerful tool for overcoming the computational limitations of traditional ab initio MD approaches. Collectively, these studies highlight the importance of computational modeling in optimizing $BaTiO_3$-based photocatalysts. However, challenges such as

 doi:10.20944/preprints202506.0553.v1

charge recombination, surface stability, and scalability of synthesis methods remain critical obstacles that need to be addressed for practical applications.

Future research should focus on integrating multiscale modeling techniques to bridge the gap between atomistic simulations and experimental validation. The incorporation of hybrid DFT functionals and beyond-DFT methods could improve the accuracy of electronic structure predictions, particularly for defect states and charge transport mechanisms. Additionally, the development of advanced machine learning potentials tailored for $BaTiO_3$ could further accelerate large-scale simulations and enhance predictive capabilities. Experimentally, synthesizing $BaTiO_3$-based heterostructures with co-catalysts and optimizing defect engineering strategies will be crucial for improving catalytic performance. A deeper exploration of photoelectrochemical and piezo-photocatalytic effects in $BaTiO_3$ could unlock new pathways for enhancing efficiency. Overall, a synergistic approach combining computational modeling and experimental techniques will be essential to realize the full potential of $BaTiO_3$ for sustainable hydrogen production.

Author Contributions: A.U.A, U.Z.T. and B.M.S.: conceptualization, methodology, formal analysis, writing—original draft, review and editing; T.M.I.: funding acquisition, writing—original draft, review and editing; M.K.: conceptualization, visualization, writing—review and editing; F.U.A.: conceptualization, formal analysis, writing— original draft, review and editing; A. I. P.: funding acquisition, writing—review and editing. All authors have read and agreed to the published version of the manuscript.

Funding: This research was funded by the Science Committee of the Ministry of Science and Higher Education of the Republic of Kazakhstan "Development of hybrid perovskite nanostructures for hydrogen photogeneration" (Grant No. AP23489103).This research was also funded by the Science Committee of the Ministry of Science and Higher Education of the Republic of Kazakhstan "Green Energy: Foundational Research of Solar Fuel Technologies for Sustainable Production and Advanced Storage" (Grant No.BR21882185).

Institutional Review Board Statement: Not applicable.

Informed Consent Statement: Not applicable.

Data Availability Statement: The raw data supporting the conclusions of this article will be made available by the authors on request.

Acknowledgments: This research was funded by the Science Committee of the Ministry of Science and Higher Education of the Republic of Kazakhstan "Development of hybrid perovskite nanostructures for hydrogen photogeneration" (Grant No. AP23489103). This research was also funded by the Science Committee of the Ministry of Science and Higher Education of the Republic of Kazakhstan "Green Energy: Foundational Research of Solar Fuel Technologies for Sustainable Production and Advanced Storage" (Grant No.BR21882185).

Conflicts of Interest: The authors declare no conflicts of interest.

Abbreviations

The following abbreviations are used in this manuscript:

CV	Conduction band
DFT	Density Functional Theory
MD	Molecular Dynamics
MLP	Machine learning potentials
SMR	Steam methane reforming
VB	Valence band

 doi:10.20944/preprints202506.0553.v1

References

1. Atilhan, S.; Park, S.; El-Halwagi, M.M.; Atilhan, M.; Moore, M.; Nielsen, R.B. Green hydrogen as an alternative fuel for the shipping industry. *Curr. Opin. Chem. Eng*.**2021**,*31*, 100668.https://doi.org/10.1016/j.coche.2020.100668
2. Qazi, U.Y. Future of hydrogen as an alternative fuel for next-generation industrial applications; challenges and expected opportunities. *Energies***2022**,*15*, 4741.https://doi.org/10.3390/en15134741
3. Hosseini, S.E.; Wahid, M.A. Hydrogen production from renewable and sustainable energy resources: Promising green energy carrier for clean development. *Renew. Sustain. Energy Rev*.**2016**, *57*, 850–866.https://doi.org/10.1016/j.rser.2015.12.112
4. Kaiwen, L.; Bin, Y.; Tao, Z. Economic analysis of hydrogen production from steam reforming process: A literature review. *Energy Sources, Part B***2018**, *13*, 109–115.https://doi.org/10.1080/15567249.2017.1387619
5. Franchi, G.; Capocelli, M.; De Falco, M.; Piemonte, V.; Barba, D. Hydrogen production via steam reforming: A critical analysis of MR and RMM technologies. *Membranes***2020**, *10*, 10.https://doi.org/10.3390/membranes10010010
6. Ranjekar, A.M.; Yadav, G.D. Steam reforming of methanol for hydrogen production: A critical analysis of catalysis, processes, and scope. *Ind. Eng. Chem. Res.***2021**, *60*, 89–113.https://doi.org/10.1021/acs.iecr.0c05041
7. Wang, M.; Wang, Z.; Gong, X.; Guo, Z. The intensification technologies to water electrolysis for hydrogen production–A review. *Renew. Sustain. Energy Rev*.**2014**, *29*, 573–588.https://doi.org/10.1016/j.rser.2013.08.090
8. El-Shafie, M. Hydrogen production by water electrolysis technologies: A review. *Results Eng*. **2023**, *20*, 101426.https://doi.org/10.1016/j.rineng.2023.101426
9. Shayan, E.; Zare, V.; Mirzaee, I.J.E.C. Hydrogen production from biomass gasification; a theoretical comparison of using different gasification agents. *Energy Convers. Manag*. **2018**, *159*, 30–41.https://doi.org/10.1016/j.enconman.2017.12.096
10. Tezer, Ö.; Karabağ, N.; Öngen, A.; Çolpan, C.Ö.; Ayol, A. Biomass gasification for sustainable energy production: A review. *Int. J. Hydrog. Energy***2022**, 47, 15419–15433.https://doi.org/10.1016/j.ijhydene.2022.02.158
11. Akhlaghi, N.; Najafpour-Darzi, G. A comprehensive review on biological hydrogen production. *Int. J. Hydrog. Energy***2020**, *45*, 22492–22512.https://doi.org/10.1016/j.ijhydene.2020.06.182
12. Xu, X.; Zhou, Q.; Yu, D. The future of hydrogen energy: Bio-hydrogen production technology. *Int. J. Hydrog. Energy***2022**, *47*, 33677–33698.https://doi.org/10.1016/j.ijhydene.2022.07.261
13. Razi, F.; Dincer, I.; Gabriel, K. Exergoenvironmental analysis of the integrated copper-chlorine cycle for hydrogen production. *Energy* **2021**, *226*, 120426.https://doi.org/10.1016/j.energy.2021.120426
14. Strušnik, D.; Avsec, J. Exergoeconomic machine-learning method of integrating a thermochemical Cu–Cl cycle in a multigeneration combined cycle gas turbine for hydrogen production. *Int. J. Hydrog. Energy* **2022**, *47*, 17121–17149.
15. https://doi.org/10.1016/j.ijhydene.2022.03.230
16. Song, H.; Luo, S.; Huang, H.; Deng, B.; Ye, J. Solar-driven hydrogen production: Recent advances, challenges, and future perspectives. *ACS Energy Lett*.**2022**, *7*, 1043–1065.https://doi.org/10.1021/acsenergylett.1c02591
17. Takeda, S.; Nam, H.; Chapman, A. Low-carbon energy transition with the sun and forest: Solar-driven hydrogen production from biomass. *Int. J. Hydrog. Energy***2022**, *47*, 24651–24668.https://doi.org/10.1016/j.ijhydene.2021.11.203
18. Lim, Y.; Lee, D.-K.; Kim, S.M.; Park, W.; Cho, S.Y.; Sim, U. Low Dimensional Carbon-Based Catalysts for Efficient Photocatalytic and Photo/Electrochemical Water Splitting Reactions. *Materials* **2020**, *13*, 114. https://doi.org/10.3390/ma13010114
19. Eidsvåg, H.; Bentouba, S.; Vajeeston, P.; Yohi, S.; Velauthapillai, D. TiO_2 as a Photocatalyst for Water Splitting—An Experimental and Theoretical Review. *Molecules* **2021**, *26*, 1687. https://doi.org/10.3390/molecules26061687
20. Nadeem, M.A.; Khan, M.A.; Ziani, A.A.; Idriss, H. An Overview of the Photocatalytic Water Splitting over Suspended Particles. *Catalysts* **2021**, *11*, 60. https://doi.org/10.3390/catal11010060

 doi:10.20944/preprints202506.0553.v1

21. Arunachalam, P.; Nagai, K.; Amer, M.S.; Ghanem, M.A.; Ramalingam, R.J.; Al-Mayouf, A.M. Recent Developments in the Use of Heterogeneous Semiconductor Photocatalyst Based Materials for a Visible-Light-Induced Water-Splitting System—A Brief Review. *Catalysts* **2021**, *11*, 160. https://doi.org/10.3390/catal11020160
22. Tian, L.; Guan, X.; Zong, S.; Dai, A.; Qu, J. Cocatalysts for Photocatalytic Overall Water Splitting: A Mini Review. *Catalysts* **2023**, *13*, 355. https://doi.org/10.3390/catal13020355
23. Jakhar, M.; Kumar, A.; Ahluwalia, P.K.; Tankeshwar, K.; Pandey, R. Engineering 2D Materials for Photocatalytic Water-Splitting from a Theoretical Perspective. *Materials* **2022**, *15*, 2221. https://doi.org/10.3390/ma15062221
24. Dauletbekova, A.; Abuova, F.; Piskunov, S. First-principles modeling of the H color centers in MgF_2 crystals. **Phys. Status Solidi C***2012*, **10**, 160–164. https://doi.org/10.1002/pssc.201200474.
25. Abuova, F.U.; Kotomin, E.A.; Lisitsyn, V.M.; Akilbekov, A.T.; Piskunov, S. Ab initio modeling of radiation damage in MgF_2 crystals. **Nucl. Instrum. Methods Phys. Res. B***2014*, **326**, 314–317. https://doi.org/10.1016/j.nimb.2013.09.027.
26. Goumri-Said, S.; Kanoun, M.B. Insight into the Effect of Anionic–Anionic Co-Doping on $BaTiO_3$ for Visible Light Photocatalytic Water Splitting: A First-Principles Hybrid Computational Study. *Catalysts* **2022**, *12*, 1672. https://doi.org/10.3390/catal12121672
27. Guo, S.; Lin, H.; Hu, J.; Su, Z.; Zhang, Y. Computational Study of Novel Semiconducting Sc_2CT_2 (T = F, Cl, Br) MXenes for Visible-Light Photocatalytic Water Splitting. *Materials* **2021**, *14*, 4739. https://doi.org/10.3390/ma14164739
28. Wang, G.; Xie, W.; Guo, S.; Chang, J.; Chen, Y.; Long, X.; Zhou, L.; Ang, Y.S.; Yuan, H. Two-Dimensional GeC/MXY (M = Zr, Hf; X, Y = S, Se) Heterojunctions Used as Highly Efficient Overall Water-Splitting Photocatalysts. *Molecules* **2024**, *29*, 2793. https://doi.org/10.3390/molecules29122793
29. Wang, Y.; Wang, H.; Li, Y.; Zhang, M.; Zheng, Y. Designing a 0D/1D S-Scheme Heterojunction of Cadmium Selenide and Polymeric Carbon Nitride for Photocatalytic Water Splitting and Carbon Dioxide Reduction. *Molecules* **2022**, *27*, 6286. https://doi.org/10.3390/molecules27196286
30. Yan, Y.; Chen, Z.; Cheng, X.; Shi, W. Research Progress of $ZnIn_2S_4$-Based Catalysts for Photocatalytic Overall Water Splitting. *Catalysts* **2023**, *13*, 967. https://doi.org/10.3390/catal13060967
31. Zhang, H.; Liu, J.; Xu, T.; Ji, W.; Zong, X. Recent Advances on Small Band Gap Semiconductor Materials (≤2.1 eV) for Solar Water Splitting. *Catalysts* **2023**, *13*, 728. https://doi.org/10.3390/catal13040728
32. Morante, N.; Folliero, V.; Dell'Annunziata, F.; Capuano, N.; Mancuso, A.; Monzillo, K.; Galdiero, M.; Sannino, D.; Franci, G. Characterization and Photocatalytic and Antibacterial Properties of Ag- and TiO_x-Based (x = 2, 3) Composite Nanomaterials under UV Irradiation. *Materials* **2024**, *17*, 2178. https://doi.org/10.3390/ma17102178
33. Zhao, Z.; Li, R.; Zhao, C.; Pei, J. A Study on the Effect of Conductive Particles on the Performance of Road-Suitable Barium Titanate/Polyvinylidene Fluoride Composite Materials. *Materials* **2025**, *18*, 1185. https://doi.org/10.3390/ma18051185
34. Mamani Flores, E.; Vera Barrios, B.S.; HuillcaHuillca, J.C.; Chacaltana García, J.A.; Polo Bravo, C.A.; Nina Mendoza, H.E.; Quispe Cohaila, A.B.; Gamarra Gómez, F.; Tamayo Calderón, R.M.; Fora Quispe, G.d.L.; et al. Cr^{3+} Doping Effects on Structural, Optical, and Morphological Characteristics of $BaTiO_3$ Nanoparticles and Their Bioactive Behavior. *Crystals* **2024**, *14*, 998. https://doi.org/10.3390/cryst14110998
35. Abidin, M. Z. U.; Ikram, M.; Moeen, S.; Nazir, G.; Kanoun, M. B.; Goumri-Said, S. A comprehensive review on the synthesis of ferrite nanomaterials via bottom-up and top-down approaches: Advantages, disadvantages, characterizations, and computational insights. *Coord. Chem. Rev.***2024**, *520*, 216158.https://doi.org/10.1016/j.ccr.2024.216158
36. Jiang, Q.; Cui, X.F.; Zhao, M. Size effects on Curie temperature of ferroelectric particles. *Appl. Phys. A Mater. Sci. Process.* **2004**, *78*, 703–704.https://doi.org/10.1016/0038-1098(94)90490-1
37. Sood, A.; Desseigne, M.; Dev, A.; Maurizi, L.; Kumar, A.; Millot, N.; Han, S.S. A Comprehensive Review on Barium Titanate Nanoparticles as a Persuasive Piezoelectric Material for Biomedical Applications: Prospects and Challenges. *Small* **2023**, *19*, e2206401. https://doi.org/10.1002/smll.202206401

 doi:10.20944/preprints202506.0553.v1

38. Lang, X.Y.; Jiang, Q. Size and interface effects on Curie temperature of perovskite ferroelectric nanosolids. *J. Nanopart. Res.* **2007**, *9*, 595–603. https://doi.org/10.1007/s11051-005-9066-1
39. Wada, S.; Hoshina, T.; Yasuno, H.; Ohishi, M.; Kakemoto, H.; Tsurumi, T.; Yashima, M. Size Effect of Dielectric Properties for Barium Titanate Particles and Its Model. *Key Eng. Mater.* **2006**, *301*, 27–30. https://doi.org/10.4028/www.scientific.net/KEM.301.27
40. Chakraborty, A.; Liton, M. N. H.; Sarker, M. S. I.; Rahman, M. M.; Khan, M. K. R. A comprehensive DFT evaluation of catalytic and optoelectronic properties of $BaTiO_3$ polymorphs. Phys. B: Condens. Matter **2023**, *648*, 414418.https://doi.org/10.1016/j.physb.2022.414418
41. Navas, D.; Fuentes, S.; Castro-Alvarez, A.; Chavez-Angel, E. Review on Sol-Gel Synthesis of Perovskite and Oxide Nanomaterials. *Gels* **2021**, *7*, 275. https://doi.org/10.3390/gels7040275
42. Lu, W.; Quilitz, M.; Schmidt, H. Nanoscaled $BaTiO_3$ powders with a large surface area synthesized by precipitation from aqueous solutions: Preparation, characterization and sintering. *J. Eur. Ceram. Soc.* **2007**, *27*, 3149–3159.https://doi.org/10.1016/j.jeurceramsoc.2007.01.002
43. Suherman, B.; Nurosyid, F.; Khairuddin; Sandi, D.K.; Irian, Y. Impacts of low sintering temperature on microstructure, atomic bonds, and dielectric constant of barium titanate ($BaTiO_3$) prepared by co-precipitation technique. *J. Phys. Conf. Ser.* **2022**, *2190*, 12006. https://doi.org/10.1088/1742-6596/2190/1/012006
44. Hayashi, H.; Hakuta, Y. Hydrothermal Synthesis of Metal Oxide Nanoparticles in Supercritical Water. *Materials* 2010, *3*, 3794–3817.https://doi.org/10.3390/ma3073794
45. Khort, A.A.; Podbolotov, K.B. Preparation of $BaTiO_3$ nanopowders by the solution combustion method. *Ceram. Int.* **2016**, *42*, 15343–15348.https://doi.org/10.1016/j.ceramint.2016.06.178
46. Choi, G.J.; Kim, H.S.; Cho, Y.S. $BaTiO_3$ particles prepared by microwave-assisted hydrothermal reaction using titanium acylate precursors. *Mater. Lett.* **1999**, *41*, 122–127. https://doi.org/10.1016/S0167-577X(99)00117-2
47. Buscaglia, V.; Buscaglia, M.T.; Canu, G. $BaTiO_3$-Based Ceramics: Fundamentals, Properties and Applications. Encyclopedia of Materials: Technical Ceramics and Glasses; Elsevier: Amsterdam, The Netherlands, 2021; pp. 311–344. ISBN 9780128222331.
48. Ramakanth, S.; James Raju, K.C. Band gap narrowing in $BaTiO_3$ nanoparticles facilitated by multiple mechanisms. *J. Appl. Phys.* **2014**, *115*, 173507.https://doi.org/10.1063/1.4871776
49. Tewatia, K.; Sharma, A.; Sharma, M.; Kumar, A. Factors affecting morphological and electrical properties of Barium Titanate: A brief review. *Mater. Today Proc.* **2021**, *44*, 4548–4556.https://doi.org/10.1016/j.matpr.2020.10.813
50. Kumar, A.; Gori, Y.; Kumar, A.; Meena, C.S.; Dutt, N. (Eds.) *Advanced Materials for Biomedical Applications*, 1st ed.; Taylor and Francis: Boca Raton, FL, USA, 2023; ISBN 9781032356068.
51. Benyoussef, M.; Mura, T.; Saitzek, S.; Azrour, F.; Blach, J.-F.; Lahmar, A.; Gagou, Y.; El Marssi, M.; Sayede, A.; Jouiad, M. Nanostructured $BaTi_{1-x}Sn_xO_3$ ferroelectric materials for electrocaloric applications and energy performance. *Curr. Appl. Phys.* **2022**, *38*, 59–66. https://doi.org/10.1016/j.cap.2022.03.012
52. Qiao, L.; Bi, X. Microstructure and grain size dependence of ferroelectric properties of $BaTiO_3$ thin films on $LaNiO_3$ buffered Si. *J. Eur. Ceram. Soc.* **2009**, *29*, 1995–2001.https://doi.org/10.1016/j.jeurceramsoc.2008.11.017
53. Buscaglia, M.T.; Buscaglia, V.; Viviani, M.; Nanni, P.; Hanuskova, M. Influence of foreign ions on the crystal structure of $BaTiO_3$. *J. Eur. Ceram. Soc.* **2000**, *20*, 1997–2007. https://doi.org/10.1016/S0955-2219(00)00076-5
54. Khedhri, M.H.; Abdelmoula, N.; Khemakhem, H.; Douali, R.; Dubois, F. Structural, spectroscopic and dielectric properties of Ca-doped $BaTiO_3$. *Appl. Phys. A Mater. Sci. Process.* **2019**, *125*, 193. https://doi.org/10.1007/s00339-019-2487-y
55. Da Lu, Y.; Han, D.D.; Liu, Q.L.; Wang, Y.D.; Sun, X.Y. Structure and Dielectric Properties of Ce and Ca Co-Doped $BaTiO_3$ Ceramics. *Key Eng. Mater.* 2016, *680*, 184–188. https://doi.org/10.4028/www.scientific.net/KEM.680.184
56. Rached, A.; Wederni, M.A.; Belkahla, A.; Dhahri, J.; Khirouni, K.; Alaya, S.; Martín-Palma, R.J. Effect of doping in the physico-chemical properties of $BaTiO_3$ ceramics. *Phys. B Condens. Matter* **2020**, *596*, 412343.https://doi.org/10.1016/j.physb.2020.412343

 doi:10.20944/preprints202506.0553.v1

57. Banerjee, T.; Balasubramanian, G. Predictive Modeling of Molecular Mechanisms in Hydrogen Production and Storage Materials. *Materials* **2023**, *16*, 6050. https://doi.org/10.3390/ma16176050
58. Inerbaev, T.M.; Abuova, A.U.; Zakiyeva, Z.Y.; Abuova, F.U.; Mastrikov, Y.A.; Sokolov, M.; Gryaznov, D.; Kotomin, E.A. Effect of Rh doping on optical absorption and oxygen evolution reaction activity on $BaTiO_3$ (001) surfaces. **Molecules** *2024*, **29**, 11. https://doi.org/10.3390/molecules29112707.
59. Chen, L.; Yu, Z.; Ji, X.; Huang, R.; Luo, L.; Tang, Z.; Zhang, Y. Insight into the effect of pH on the ferroelectric polarization field applied in photoelectrochemical water oxidation. *Mater. Sci. Semicond. Process.***2022**, *147*, 106729. https://doi.org/10.1016/j.mssp.2022.106729
60. Boonpalit, K., &Artrith, N. (2024). Mechanistic Insights into the Oxygen Evolution Reaction on Nickel-Doped Barium Titanate via Machine Learning-Accelerated Simulations. *arXiv preprint arXiv:2412.15452*.https://doi.org/10.48550/arXiv.2412.15452
61. Bradley, R.; Radhakrishnan, R. Coarse-Grained Models for Protein-Cell Membrane Interactions. *Polymers* **2013**, *5*, 890-936. https://doi.org/10.3390/polym5030890
62. Ren, H.; Yang, J.; Yang, W.; Zhong, H.; Lin, J.; Radjenovic, P. M.; Sun, L.; Zhang, H.; Xu, J.; Tian, Z.; Li, J. Core–Shell–Satellite plasmonic photocatalyst for broad-spectrum photocatalytic water splitting. *ACS Mater. Lett.***2020**, *3*, 69–76. https://doi.org/10.1021/acsmaterialslett.0c00479
63. Goga, N.; Mayrhofer, L.; Tranca, I.; Nedea, S.; Heijmans, K.; Ponnuchamy, V.; Vasilateanu, A. A Review of Recent Developments in Molecular Dynamics Simulations of the Photoelectrochemical Water Splitting Process. *Catalysts* **2021**, *11*, 807. https://doi.org/10.3390/catal11070807
64. Abdikarimova, U.; Bissenova, M.; Matsko, N.; Issadykov, A.; Khromushin, I.; Aksenova, T.; Munasbayeva, K.; Slyamzhanov, E.; Serik, A. Visible Light-Driven Photocatalysis of Al-Doped $SrTiO_3$: Experimental and DFT Study. *Molecules* **2024**, *29*, 5326. https://doi.org/10.3390/molecules29225326
65. Eglitis, R.I.; Piskunov, S.; Popov, A.I.; Purans, J.; Bocharov, D.; Jia, R. Systematic Trends in Hybrid-DFT Computations of $BaTiO_3/SrTiO_3$, $PbTiO_3/SrTiO_3$ and $PbZrO_3/SrZrO_3$ (001) Hetero Structures. *Condens. Matter* **2022**, *7*, 70. https://doi.org/10.3390/condmat7040070
66. Eglitis, R.I.; Purans, J.; Jia, R. Comparative Hybrid Hartree-Fock-DFT Calculations of WO_2-Terminated Cubic WO_3 as Well as $SrTiO_3$, $BaTiO_3$, $PbTiO_3$ and $CaTiO_3$ (001) Surfaces. *Crystals* **2021**, *11*, 455. https://doi.org/10.3390/cryst11040455
67. Sikam, P.; Thirayatorn, R.; Kaewmaraya, T.; Thongbai, P.; Moontragoon, P.; Ikonic, Z. Improved Thermoelectric Properties of $SrTiO_3$ via (La, Dy and N) Co-Doping: DFT Approach. *Molecules* **2022**, *27*, 7923. https://doi.org/10.3390/molecules27227923
68. Eglitis, R.I.; Jia, R. Review of Systematic Tendencies in (001), (011) and (111) Surfaces Using B3PW as Well as B3LYP Computations of $BaTiO_3$, $CaTiO_3$, $PbTiO_3$, $SrTiO_3$, $BaZrO_3$, $CaZrO_3$, $PbZrO_3$ and $SrZrO_3$ Perovskites. *Materials* **2023**, *16*, 7623. https://doi.org/10.3390/ma16247623
69. Jouybar, S.; Naji, L.; Sarabadani Tafreshi, S.; de Leeuw, N.H. A Density Functional Theory Study of the Physico-Chemical Properties of Alkali Metal Titanate Perovskites for Solar Cell Applications. *Molecules* **2024**, *29*, 3355. https://doi.org/10.3390/molecules29143355
70. Elegbeleye, I.F.; Maluta, N.E.; Maphanga, R.R. Density Functional Theory Study of Optical and Electronic Properties of $(TiO_2)_{n=5,8,68}$ Clusters for Application in Solar Cells. *Molecules* **2021**, *26*, 955. https://doi.org/10.3390/molecules26040955
71. Yan, Z.; Zhang, Y.; Kang, W.; Deng, N.; Pan, Y.; Sun, W.; Ni, J.; Kang, X. TiO_2 Gas Sensors Combining Experimental and DFT Calculations: A Review. *Nanomaterials* **2022**, *12*, 3611. https://doi.org/10.3390/nano12203611
72. Gustavsen, K.R.; Feng, T.; Huang, H.; Li, G.; Narkiewicz, U.; Wang, K. DFT Calculation of Carbon-Doped TiO_2 Nanocomposites. *Materials* **2023**, *16*, 6117. https://doi.org/10.3390/ma16186117
73. Wang, J.; Zhou, T.; Zhang, Y.; Chen, S.; Bai, J.; Li, J.; Zhou, B. The design of high-performance photoanode of $CQDs/TiO_2/WO_3$ based on DFT alignment of lattice parameter and energy band, and charge distribution. *J. Colloid Interface Sci.***2021**, *600*, 828–837.https://doi.org/10.1016/j.jcis.2021.05.086
74. Thongyong, N.; Chanlek, N.; Srepusharawoot, P.; Takesada, M.; Cann, D. P.; Thongbai, P. Experimental study and DFT calculations of improved giant dielectric properties of Ni^{2+}/Ta^{5+} co-doped TiO_2 by

 doi:10.20944/preprints202506.0553.v1

engineering defects and internal interfaces. *J. Eur. Ceram. Soc.***2022**, *42*, 4944–4952.https://doi.org/10.1016/j.jeurceramsoc.2022.05.037

75. Amrhar, O.; Lee, H. S.; Lgaz, H.; Berisha, A.; Ebenso, E. E.; Cho, Y. Computational insights into the adsorption mechanisms of anionic dyes on the rutile TiO_2 (110) surface: Combining SCC-DFT tight binding with quantum chemical and molecular dynamics simulations. *J. Mol. Liq.***2023**, *377*, 121554.https://doi.org/10.1016/j.molliq.2023.121554
76. Zeng, Z.; Wodaczek, F.; Liu, K.; Stein, F.; Hutter, J.; Chen, J.; Cheng, B. Mechanistic insight on water dissociation on pristine low-index TiO_2 surfaces from machine learning molecular dynamics simulations. *Nat. Commun.***2023**, *14*, 6131.https://doi.org/10.1038/s41467-023-41865-8
77. Boboriko, N. E.; Dzichenka, Y. U. Molecular dynamics simulation as a tool for prediction of the properties of TiO_2 and TiO_2: MoO_3-based chemical gas sensors. *J. Alloys Compd.***2021**, *855*, 157490.https://doi.org/10.1016/j.jallcom.2020.157490
78. Raffaini, G. Surface chemistry, crystal structure, size, and topography role in the albumin adsorption process on TiO_2 anatase crystallographic faces and its 3D-nanocrystal: A molecular dynamics study. *Coatings* 2021, *11*, 420.https://doi.org/10.3390/coatings11040420
79. Maleki, F.; Di Liberto, G.; Pacchioni, G. pH-and facet-dependent surface chemistry of TiO_2 in aqueous environment from first principles. *ACS Appl. Mater. Interfaces***2023**, *15*, 11216–11224.https://doi.org/10.1021/acsami.2c19273
80. Nosaka, Y. Water Photo-Oxidation over TiO_2—History and Reaction Mechanism. *Catalysts* **2022**, *12*, 1557. https://doi.org/10.3390/catal12121557
81. Estévez Ruiz, E.P.; Lago, J.L.; Thirumuruganandham, S.P. Experimental Studies on TiO_2 NT with Metal Dopants through Co-Precipitation, Sol–Gel, Hydrothermal Scheme and Corresponding Computational Molecular Evaluations. *Materials* **2023**, *16*, 3076. https://doi.org/10.3390/ma16083076
82. Harrison, J.A.; Schall, J.D.; Maskey, S.; Mikulski, P.T.; Knippenberg, M.T.; Morrow, B.H. Review of force fields and intermolecular potentials used in atomistic computational materials research. *Appl. Phys. Rev.* **2018**, *5*, 031104.
83. Yang, M.; Bonati, L.; Polino, D.; Parrinello, M. Using metadynamics to build neural network potentials for reactive events: The case of urea decomposition in water. *Catal. Today* **2022**, *387*, 143–149.
84. Lowe, J.S.; Siegel, D.J. Modeling the interface between lithium metal and its native oxide. *ACS Appl. Mater. Interfaces* **2020**, *12*, 46015–46026.
85. Joraleechanchai, N.; Duangdangchote, S.; Sawangphruk, M. Machine Learning and Reactive Force Field Molecular Dynamics Investigation of Electrolytes for Ultra-fast Charging Li-ion Batteries. *ECS Trans.* **2020**, *97*, 45.
86. Yao, N.; Chen, X.; Fu, Z.H.; Zhang, Q. Applying classical, ab initio, and machine-learning molecular dynamics simulations to the liquid electrolyte for rechargeable batteries. *Chem. Rev.* **2022**, *122*, 10970–11021.
87. Chen, Y.; Liu, Y.; Xu, Y.; Guo, X.; Cao, Y.; Ming, W. Review: Modeling and Simulation of Membrane Electrode Material Structure for Proton Exchange Membrane Fuel Cells. *Coatings* **2022**, *12*, 1145. https://doi.org/10.3390/coatings12081145
88. Samantaray, S.; Mohanty, D.; Satpathy, S.K.; Hung, I.-M. Exploring Recent Developments in Graphene-Based Cathode Materials for Fuel Cell Applications: A Comprehensive Overview. *Molecules* **2024**, *29*, 2937. https://doi.org/10.3390/molecules29122937
89. Dhanasekaran, A.; Subramanian, Y.; Omeiza, L.A.; Raj, V.; Yassin, H.P.H.M.; SA, M.A.; Azad, A.K. Computational Fluid Dynamics for Protonic Ceramic Fuel Cell Stack Modeling: A Brief Review. *Energies* **2023**, *16*, 208. https://doi.org/10.3390/en16010208
90. Wang, W.; Qu, Z.; Wang, X.; Zhang, J. A Molecular Model of PEMFC Catalyst Layer: Simulation on Reactant Transport and Thermal Conduction. *Membranes* **2021**, *11*, 148. https://doi.org/10.3390/membranes11020148
91. Chen, X.; Hou, W.; Zhai, F.; Cheng, J.; Yuan, S.; Li, Y.; Wang, N.; Zhang, L.; Ren, J. Reversible Hydrogen Storage Media by g-CN Monolayer Decorated with NLi_4: A First-Principles Study. *Nanomaterials* **2023**, *13*, 647. https://doi.org/10.3390/nano13040647

 doi:10.20944/preprints202506.0553.v1

92. Li, Q.; Li, Q.; Wang, F.; Wu, J.; Wang, Y. The Carrying Behavior of Water-Based Fracturing Fluid in Shale Reservoir Fractures and Molecular Dynamics of Sand-Carrying Mechanism. *Processes* **2024**, *12*, 2051. https://doi.org/10.3390/pr12092051
93. Hu, Z.; Wei, L. Review on Characterization of Biochar Derived from Biomass Pyrolysis via Reactive Molecular Dynamics Simulations. *J. Compos. Sci.* **2023**, *7*, 354. https://doi.org/10.3390/jcs7090354
94. Shelyapina, M.G. Hydrogen Diffusion on, into and in Magnesium Probed by DFT: A Review. *Hydrogen* **2022**, *3*, 285-302. https://doi.org/10.3390/hydrogen3030017
95. Mutisya, S. M., &Kalinichev, A. G. (2021). Carbonation reaction mechanisms of portlandite predicted from enhanced Ab Initio molecular dynamics simulations. *Minerals*, *11*(5), 509.https://doi.org/10.3390/min11050509
96. Kohmuean, P.; Inthomya, W.; Wongkoblap, A.; Tangsathitkulchai, C. Monte Carlo Simulation and Experimental Studies of CO_2, CH_4 and Their Mixture Capture in Porous Carbons. *Molecules* **2021**, *26*, 2413. https://doi.org/10.3390/molecules26092413
97. Sobornova, V.V.; Belov, K.V.; Dyshin, A.A.; Gurina, D.L.; Khodov, I.A.; Kiselev, M.G. Molecular Dynamics and Nuclear Magnetic Resonance Studies of Supercritical CO_2 Sorption in Poly(Methyl Methacrylate). *Polymers* **2022**, *14*, 5332. https://doi.org/10.3390/polym14235332
98. Dong, K.; Niu, Z.; Kong, S.; Jia, B. Impact of Supercritical Carbon Dioxide on Pore Structure and Gas Transport in Bituminous Coal: An Integrated Experiment and Simulation. *Molecules* **2025**, *30*, 1200. https://doi.org/10.3390/molecules30061200
99. Filipe, H.A.L.; Loura, L.M.S. Molecular Dynamics Simulations: Advances and Applications. *Molecules* **2022**, *27*, 2105. https://doi.org/10.3390/molecules27072105
100. Smith, A.; Dong, X.; Raghavan, V. An Overview of Molecular Dynamics Simulation for Food Products and Processes. *Processes* **2022**, *10*, 119. https://doi.org/10.3390/pr10010119
101. Celik, I.; Yadav, R.; Duzgun, Z.; Albogami, S.; El-Shehawi, A.M.; Fatimawali; Idroes, R.; Tallei, T.E.; Emran, T.B. Interactions of the Receptor Binding Domain of SARS-CoV-2 Variants with hACE2: Insights from Molecular Docking Analysis and Molecular Dynamic Simulation. *Biology* **2021**, *10*, 880. https://doi.org/10.3390/biology10090880
102. SdfLiu, W.D.; Yu, Y.; Dargusch, M.; Liu, Q.; Chen, Z.G. Carbon allotrope hybrids advance thermoelectric development and applications. *Renew. Sustain. Energy Rev.* **2021**, *141*, 110800.https://doi.org/10.1016/j.rser.2021.110800
103. Zhang, Y.Q.; Liu, Y.J.; Liu, Y.L.; Zhao, J.X. Boosting sensitivity of Boron Nitride Nanotube (BNNT) to nitrogen dioxide by Fe encapsulation. *J. Mol. Graph. Model.* **2014**, *51*, 1–6.https://doi.org/10.1016/j.jmgm.2014.04.005
104. Rodríguez-Quintana, R.; Carbajal-Franco, G.; Rojas-Chávez, H. DFT study of the H_2 molecules adsorption on pristine and Ni doped graphite surfaces. *Mater. Lett.* **2021**, *293*, 129660.https://doi.org/10.1016/j.matlet.2021.129660
105. Zhang, W.-S.; Liu, Y.-T.; Yao, T.-T.; Wu, G.-P.; Liu, Q. Oxygen defect engineering toward the length-selective tailoring of carbon nanotubes via a two-step electrochemical strategy. *J. Phys. Chem. C* **2020**, *124*, 27097–27106.https://doi.org/10.1021/acs.jpcc.0c07699
106. Elias, A.; Uddin, N.; Hossain, A.; Saha, J.K.; Siddiquey, I.A.; Sarker, D.R.; Diba, Z.R.; Uddin, J.; Choudhury, M.H.R.; Firoz, S.H. An experimental and theoretical study of the effect of Ce doping in ZnO/CNT composite thin film with enhanced visible light photo-catalysis. Int. J. Hydrogen Energy 2019, 44, 20068–20078.https://doi.org/10.1016/j.ijhydene.2019.06.056
107. Liu, Y.; Zhang, H.; Zhang, Z.; Jia, X.; An, L. CO adsorption on Fe-doped vacancy-defected CNTs–A DFT study. *Chem. Phys. Lett.* **2019**, *730*, 316–320.https://doi.org/10.1016/j.cplett.2019.06.013
108. Jakhar, M.; Kumar, A.; Ahluwalia, P.K.; Tankeshwar, K.; Pandey, R. Engineering 2D Materials for Photocatalytic Water-Splitting from a Theoretical Perspective. *Materials* **2022**, *15*, 2221. https://doi.org/10.3390/ma15062221
109. Xu, J.; Wan, Q.; Anpo, M.; Lin, S. Bandgap opening of graphdiyne monolayer via B, N-codoping for photocatalytic overall water splitting: Design strategy from DFT studies. *J. Phys. Chem. C* **2020**, *124*, 6624–6633. https://doi.org/10.1021/acs.jpcc.9b11385

 doi:10.20944/preprints202506.0553.v1

110. Loh, G.; Pandey, R.; Yap, Y.K.; Karna, S.P. MoS2 quantum dot: Effects of passivation, additional layer, and h-BN substrate on its stability and electronic properties. *J. Phys. Chem. C* **2015**, *119*, 1565–1574. https://doi.org/10.1021/jp510598x
111. Pandey, D.; Kumar, A.; Chakrabarti, A.; Pandey, R. Stacking-dependent electronic properties of aluminene based multilayer van der Waals heterostructures. *Comput. Mater. Sci.* **2020**, *185*, 109952.https://doi.org/10.1016/j.commatsci.2020.109952
112. Lin, Y.-P.; Bocharov, D.; Isakoviča, I.; Pankratov, V.; Popov, A.A.; Popov, A.I.; Piskunov, S. Chlorine Adsorption on TiO_2(110)/Water Interface: Nonadiabatic Molecular Dynamics Simulations for Photocatalytic Water Splitting. *Electron. Mater.* **2023**, *4*, 33-48. https://doi.org/10.3390/electronicmat4010004
113. Tada, K.; Sakata, K.; Yamada, S.; Okazaki, K.; Kitagawa, Y.; Kawakami, T.; Yamanaka, S.; Okumura, M. DFT calculations for Au adsorption onto a reduced TiO_2 (110) surface with the coexistence of Cl. *Mol. Phys.* **2014**, *112*, 365–378.https://doi.org/10.1080/00268976.2013.822113
114. Li, Y.; Gao, D.; Peng, S.; Lu, G.; Li, S. Photocatalytic hydrogen evolution over Pt/$Cd_{0.5}Zn_{0.5}S$ from saltwater using glucose as electron donor: An investigation of the influence of electrolyte NaCl. *Int. J. Hydrog. Energy* **2011**, *36*, 4291–4297.https://doi.org/10.1016/j.ijhydene.2011.01.038
115. Alghamdi, H.; Idriss, H. Study of the modes of adsorption and electronic structure of hydrogen peroxide and ethanol over TiO_2 rutile (110) surface within the context of water splitting. *Surf. Sci.* **2018**, *669*, 103–113.https://doi.org/10.1016/j.susc.2017.09.011
116. Vu, N.H.; Le, H.V.; Cao, T.M.; Pham, V.V.; Le, H.M.; Nguyen-Manh, D. Anatase–rutile phase transformation of titanium dioxide bulk material: A DFT+U approach. *J. Phys. Condens. Matter* **2012**, *24*, 405501.https://doi.org/10.1088/0953-8984/24/40/405501
117. Kolesov, G.; Grånäs, O.; Hoyt, R.; Vinichenko, D.; Kaxiras, E. Real–time TD–DFT with classical ion dynamics: Methodology and applications. *J. Chem. Theory Comput.* **2016**, *12*, 466–476.https://doi.org/10.1021/acs.jctc.5b00969
118. You, P.; Chen, D.; Lian, C.; Zhang, C.; Meng, S. First–principles dynamics of photoexcited molecules and materials towards a quantum description. *Wiley Interdiscip. Rev. Comput. Mol. Sci.* **2021**, *11*, e1492.https://doi.org/10.1002/wcms.1492
119. Pham, T.A.; Ping, Y.; Galli, G. Modelling heterogeneous interfaces for solar water splitting. *Nat. Mater.* **2017**, *16*, 401–408.https://doi.org/10.1038/nmat4803
120. Agosta, L.; Brandt, E.G.;Lyubartsev, A.P. Diffusion and reaction pathways of water near fully hydrated TiO_2 surfaces from ab initio molecular dynamics. *J. Chem. Phys.* **2017**, *147*, 024704.https://doi.org/10.1063/1.4991381
121. Balzaretti, F.; Gupta, V.; Ciacchi, L.C.; Aradi, B.; Frauenheim, T.; Köppen, S. Water reactions on reconstructed rutile TiO_2: A density functional theory/density functional tight binding approach. *J. Phys. Chem. C* **2021**, *125*, 13234–13246. https://doi.org/10.1021/acs.jpcc.1c00871
122. Gao, M.; Connor, P.K.N.; Ho, G.W. Plasmonic photothermic directed broadband sunlight harnessing for seawater catalysis and desalination. *Energy Environ. Sci.* **2016**, *9*, 3151–3160. https://doi.org/10.1039/C6EE00971A
123. Schilling, M.; Luber, S. Computational Modeling of Cobalt-Based Water Oxidation: Current Status and Future Challenges. *Front Chem.* **2018**, *6*, 100. https://doi.org/10.3389/fchem.2018.00100
124. VandeVondele, J.; Mohamed, F.; Krack, M.; Hutter, J.; Sprik, M.; Parrinello, M. The influence of temperature and density functional models in ab initio molecular dynamics simulation of liquid water. *J. Chem. Phys.* **2005**, *122*, 014515. https://doi.org/10.1063/1.1828433
125. Sinha, V.; Govindarajan, N.; de Bruin, B.; Meijer, E.J. How Solvent Affects C–H Activation and Hydrogen Production Pathways in Homogeneous Ru-Catalyzed Methanol Dehydrogenation Reactions. *ACS Catal.* **2018**, *8*, 6908–6913.https://doi.org/10.1021/acscatal.8b01177
126. Cheng, J.; Liu, X.; VandeVondele, J.; Sulpizi, M.; Sprik, M. Redox Potentials and Acidity Constants from Density Functional Theory Based Molecular Dynamics. *Acc. Chem. Res.* **2014**, *47*, 3522–3529.https://doi.org/10.1021/ar500268y

 doi:10.20944/preprints202506.0553.v1

127. Liu, X.; Jiang, B.; Liu, Y.; Liu, L.; Xia, T.; Zhang, X.; Ye, C.; Yu, Y.; Wang, B. Two-Dimensional As/BlueP van der Waals Hetero-Structure as a Promising Photocatalyst for Water Splitting: A DFT Study. *Coatings* **2020**, *10*, 1160. https://doi.org/10.3390/coatings10121160
128. Singh, A.K.; Mathew, K.; Zhuang, H.L.; Henning, R.G. Computational screening of 2D materials for photocatalysis. *J. Phys. Chem. Lett.* **2015**, *6*, 1087–1098.https://doi.org/10.1021/jz502646d
129. Ma, X.G.; Lv, Y.H.; Xu, J.; Liu, Y.F.; Zhang, R.Q.; Zhu, Y.F. A strategy of enhancing the photoactivity of g-C3N4 via doping of nonmetal elements: A first-principles study. *J. Phys. Chem. C* **2012**, *116*, 23485–23493.https://doi.org/10.1021/jp308334x
130. Li, G.; Zhao, Y.C.; Zeng, S.M.; Ni, J. The realization of half-metal and spin-semiconductor for metal adatoms on arsenene. *Appl. Surf. Sci.* **2016**, *390*, 60–67.https://doi.org/10.1016/j.apsusc.2016.08.016
131. Li, X.H.; Wang, B.J.; Cai, X.L.; Zhang, L.W.; Wang, G.D.; Ke, S.H. Tunable electronic properties of arsenene/GaS van der Waals heterostructures. *RSC Adv.* **2017**, *7*, 28393.https://doi.org/10.1039/C7RA03748A
132. Fang, L.Z.; Li, X.P.; Geng, Z.D.; Wang, T.X.; Xia, C.X. Band alignment tuning in GeS/arsenene staggered hetero-structures. *J. Alloy. Compd.* **2019**, *793*, 283–288.https://doi.org/10.1016/j.jallcom.2019.04.145
133. Jamdagni, P.; Thakur, A.; Kumar, A.; Ahluwalia, P.K.; Pandey, R. Two dimensional allotropes of arsenene with a wide range of high and anisotropic carrier mobility. *Phys. Chem. Chem. Phys.* **2018**, *20*, 29939.https://doi.org/10.1039/C8CP06162A
134. Wang, B.J.; Li, X.H.; Cai, X.L.; Yu, W.Y.; Zhang, L.W.; Zhao, R.Q.; Ke, S.H. Blue Phosphorus/$Mg(OH)_2$ van der Waals hetero-structures as Promising Visible-Light Photocatalysts for Water Splitting. *J. Phys. Chem. C* **2018**, *122*, 7075–7080. https://doi.org/10.1021/acs.jpcc.7b12408
135. Li, Q.F.; Ma, X.F.; Lei, Z.; Wan, X.G.; Rao, W.F. Theoretical design of blue phosphorene/arsenene lateral heterostructures with superior electronic properties. *J. Phys. D Appl. Phys.* **2018**, *51*, 255304. https://doi.org/10.1088/1361-6463/aac563
136. Inerbaev, T. M., Graupner, D. R., Abuova, A. U., Abuova, F. U., & Kilin, D. S. (2025). Optical properties of $BaTiO_3$ at room temperature: DFT modelling. *RSC Advances, 15*(7), 5405–5412. https://doi.org/10.1039/D4RA06938B.
137. Ogunkunle, S.A.; Mortier, F.; Bouzid, A.; Hinsch, J.J.; Zhang, L.; Wu, Z.; Bernard, S.; Zhu, Y.; Wang, Y. Navigating Alkaline Hydrogen Evolution Reaction Descriptors for Electrocatalyst Design. *Catalysts* **2024**, *14*, 608. https://doi.org/10.3390/catal14090608
138. Miran, H.A.; Jaf, Z.N.; Altarawneh, M.; Jiang, Z.-T. An Insight into Geometries and Catalytic Applications of CeO_2 from a DFT Outlook. *Molecules* **2021**, *26*, 6485. https://doi.org/10.3390/molecules26216485
139. Yang, C., Chen, Y., Chen, T., Rajendran, S., Zeng, Z., Qin, J., & Zhang, X. (2021). A long-standing polarized electric field in TiO_2@$BaTiO_3$/CdS nanocomposite for effective photocatalytic hydrogen evolution. *Fuel, 314*, 122758. https://doi.org/10.1016/j.fuel.2021.122758
140. Cai, W., Ma, X., Chen, J., Shi, R., Wang, Y., Yang, Y., Jing, D., Yuan, H., Du, J., & Que, M. (2023). Synergy of oxygen vacancy and piezoelectricity effect promotes the CO_2 photoreduction by $BaTiO_3$. *Applied Surface Science, 619*, 156773. https://doi.org/10.1016/j.apsusc.2023.156773
141. Wang, M., Wang, C., Liu, Y., & Zhou, X. (2019). Hybrid density functional theory description of non-metal doping in perovskite $BaTiO_3$ for visible-light photocatalysis. *Journal of Solid State Chemistry, 280*, 121018. https://doi.org/10.1016/j.jssc.2019.121018
142. Rizwan, M., Hajra, N., Zeba, I., Shakil, M., Gillani, S., & Usman, Z. (2020). Electronic, structural, and optical properties of $BaTiO_3$ doped with lanthanum (La): Insight from DFT calculation. *Optik, 211*, 164611. https://doi.org/10.1016/j.ijleo.2020.164611
143. Xu, H., Wang, P., Luan, S., Cheng, L., Fu, Z., Cao, X., Zhang, L., Yu, S., & Sun, R. (2024). Vacancy engineering for high tetragonal $BaTiO_3$ synthesized by solid-state approaches. *Powder Technology, 444*, 119955. https://doi.org/10.1016/j.powtec.2024.119955
144. Xie, P., Yang, F., Li, R., Ai, C., Lin, C., & Lin, S. (2019). Improving hydrogen evolution activity of perovskite $BaTiO_3$ with Mo doping: Experiments and first-principles analysis. *International Journal of Hydrogen Energy, 44(23)*, 11695–11704. https://doi.org/10.1016/j.ijhydene.2019.03.145

 doi:10.20944/preprints202506.0553.v1

145. Usman, M., Rehman, J. U., Tahir, M. B., & Hussain, A. (2022). First-principles calculations to investigate the effect of Cs-doping in $BaTiO_3$ for water-splitting application. *Solid State Communications, 355*, 114920. https://doi.org/10.1016/j.ssc.2022.114920
146. Chun, H., Lee, Y., Kim, S., Yoon, Y., Kim, Y., & Park, S. (2021). Surface termination of $BaTiO_3$(111) single crystal: A combined DFT and XPS study. *Applied Surface Science, 578*, 152018. https://doi.org/10.1016/j.apsusc.2021.152018
147. Dahbi, S., Tahiri, N., Bounagui, O. E., &Ez-Zahraouy, H. (2022). Effects of oxygen group elements on thermodynamic stability, electronic structures, and optical properties of the pure and pressed $BaTiO_3$ perovskite. *Computational Condensed Matter, 32*, e00728. https://doi.org/10.1016/j.cocom.2022.e00728
148. Dahbi, S., Tahiri, N., Bounagui, O. E., &Ez-Zahraouy, H. (2021). Electronic, optical, and thermoelectric properties of perovskite $BaTiO_3$ compound under the effect of compressive strain. *Chemical Physics, 544*, 111105. https://doi.org/10.1016/j.chemphys.2021.111105
149. Fo, Y., & Zhou, X. (2022). A theoretical study on tetragonal $BaTiO_3$ modified by surface co-doping for photocatalytic overall water splitting. *International Journal of Hydrogen Energy, 47(44)*, 19073–19085. https://doi.org/10.1016/j.ijhydene.2022.04.098
150. Chakraborty, A., Liton, M., Sarker, M., Rahman, M., & Khan, M. (2022). A comprehensive DFT evaluation of catalytic and optoelectronic properties of $BaTiO_3$ polymorphs. *Physica B: Condensed Matter, 648*, 414418. https://doi.org/10.1016/j.physb.2022.414418
151. Bhat, D. K., Bantawal, H., Pi, U., & Shenoy, U. S. (2023). Enhanced photoresponse and efficient charge transfer in porous graphene-$BaTiO_3$ nanocomposite for high-performance photocatalysis. *Diamond and Related Materials, 139*, 110312. https://doi.org/10.1016/j.diamond.2023.110312
152. Bashir, M. Z., Naqvi, S. A. Z., Naeem, M. A., Munir, R., & Noreen, S. (2024). Theoretical study of optoelectronic, elastic, and mechanical properties of gallium-modified barium titanate ($Ba_{1-x}Ga_xTiO_3$) perovskite ceramics by DFT. *Materials Science in Semiconductor Processing, 182*, 108734. https://doi.org/10.1016/j.mssp.2024.108734
153. Wang, S., Ge, K., Cui, H., Li, S., Yang, Y., Pan, M., & Zhu, L. (2023). Self-polarization-enhanced oxygen evolution reaction by flower-like core–shell $BaTiO_3$@NiFe-layered double hydroxide heterojunctions. *Chemical Engineering Journal, 479*, 147831. https://doi.org/10.1016/j.cej.2023.147831
154. Chen, G., Ji, Y., Shi, X., An, P., Zhang, J., Li, Y., Liu, S. F., & Yan, J. (2024). Oxygen-deficient $BaTiO_3$ loading sub-nm PtO_x for photocatalytic biological wastewater splitting to green hydrogen production. *Chemical Engineering Journal, 496*, 154261. https://doi.org/10.1016/j.cej.2024.154261
155. Guo, M., Zhong, J., Li, W., Hou, H., Bowen, C. R., Zhan, X., Yang, H., Yang, M., Chen, Z., Chen, D., Liang, Z., & Yang, W. (2024). Highly efficient photocatalytic hydrogen evolution enabled by piezotronic effects in $SrTiO_3$/$BaTiO_3$ nanofiber heterojunctions. *Nano Energy, 127*, 109745. https://doi.org/10.1016/j.nanoen.2024.109745
156. Zulfiqar, W., & Alay-E-Abbas, S. M. (2022). Improved thermodynamic stability and visible light absorption in Zr+Xcodoped (X = S, Se, and Te) $BaTiO_3$ photocatalysts: A first-principles study. *Materials Today Communications, 32*, 103867. https://doi.org/10.1016/j.mtcomm.2022.103867
157. Kovač, I., Mužević, M., Pajtler, M. V., & Lukačević, I. (2023). Charge carrier dynamics across the metal oxide/$BaTiO_3$ interfaces toward photovoltaic applications from the theoretical perspective. *Surfaces and Interfaces, 39*, 102974. https://doi.org/10.1016/j.surfin.2023.102974
158. Kaptagay, G.A.; Satanova, B.M.; Abuova, A.U.; Konuhova, M.; Zakiyeva, Zh.Ye.; Tolegen, U.Zh.; Koilyk, N.O.; Abuova, F.U. Effect of rhodium doping for photocatalytic activity of barium titanate. **Opt. Mater. X** *2025*, **25**, 100382. https://doi.org/10.1016/j.omx.2024.100382.
159. Opoku, F., Akoto, O., Kwaansa-Ansah, E. E., Asare-Donkor, N. K., &Adimado, A. A. (2023). Role of $BaTiO_3$ crystal surfaces on the electronic properties, charge separation, and visible light–response of the most active (001) surface of $LaAlO_3$: A hybrid density functional study. *Chemical Physics Impact, 6*, 100236. https://doi.org/10.1016/j.chphi.2023.100236
160. Abbasi, P., Barone, M. R., De La Paz Cruz-Jáuregui, M., Valdespino-Padilla, D., Paik, H., Kim, T., Kornblum, L., Schlom, D. G., Pascal, T. A., & Fenning, D. P. Ferroelectric Modulation of Surface Electronic States in

 doi:10.20944/preprints202506.0553.v1

$BaTiO_3$ for Enhanced Hydrogen Evolution Activity. *Nano Lett.***2022**, *22*(10), 4276–4284. https://doi.org/10.1021/acs.nanolett.2c00047

161. Gunawan, M.; Bowdler, O.; Zhou, S.; Fang, X.; Zhang, Q.; Sakamoto, Y.; Sun, K.; Gunawan, D.; Chang, S. L.; Amal, R.; Valanoor, N.; Scott, J.; Hart, J. N.; Toe, C. Y. Ferroelectric Polarization-Induced Performance Enhancements in $BiFeO_3/BiVO_4$ Photoanodes for Photoelectrochemical Water Splitting. *Adv. Funct. Mater.***2025**. https://doi.org/10.1002/adfm.202417651
162. Goumri-Said, S.; Kanoun, M.B. Insight into the Effect of Anionic–Anionic Co-Doping on $BaTiO_3$ for Visible Light Photocatalytic Water Splitting: A First-Principles Hybrid Computational Study. *Catalysts* **2022**, *12*, 1672. https://doi.org/10.3390/catal12121672
163. Chandrappa, S.; Galbao, S. J.; Krishnan, P. S. S. R.; Koshi, N. A.; Das, S.; Myakala, S. N.; Lee, S.; Dutta, A.; Cherevan, A.; Bhattacharjee, S.; Murthy, D. H. K. Iridium-Doping as a Strategy to Realize Visible-Light Absorption and P-Type Behavior in $BaTiO_3$. *J. Phys. Chem. C***2023**, *127*(25), 12383–12393. https://doi.org/10.1021/acs.jpcc.3c02942.
164. Bhat, D. K.; Bantawal, H.; Shenoy, U. S. Rhodium Doping Augments Photocatalytic Activity of Barium Titanate: Effect of Electronic Structure Engineering. *Nanoscale Adv.***2020**, *2*(12), 5688–5698. https://doi.org/10.1039/d0na00702a.
165. Qiu, H.; Yang, T.; Zhou, J.; Yang, K.; Ying, Y.; Ding, K.; Yang, M.; Huang, H. Tunable Hydrogen Evolution Activity by Modulating Polarization States of Ferroelectric $BaTiO_3$. *J. Mater. Chem. A***2023**, *11*(13), 7034–7042. https://doi.org/10.1039/d2ta07907k.
166. Wang, Y.; Zhou, Q.; Zhang, Q.; Ren, Y.; Cui, K.; Cheng, C.; Wu, K. Effects of La-N Co-Doping of $BaTiO_3$ on Its Electron-Optical Properties for Photocatalysis: A DFT Study. *Molecules* **2024**, *29*, 2250. https://doi.org/10.3390/molecules29102250
167. Saadon, N. M. Q.; Miran, H. A. Optoelectronic Tuning of Barium Titanate Doped with Pt: A Systematic First-Principles Study. *Pap. Phys.***2024**, *16*, 160002. https://doi.org/10.4279/pip.160002.
168. Sharma, D.; Upadhyay, S.; Satsangi, V. R.; Shrivastav, R.; Waghmare, U. V.; Dass, S. Nanostructured $BaTiO_3/Cu_2O$ Heterojunction with Improved Photoelectrochemical Activity for H_2 Evolution: Experimental and First-Principles Analysis. *Appl. Catal., B***2016**, *189*, 75–85. https://doi.org/10.1016/j.apcatb.2016.02.037.
169. Zhao, Y.; Ran, L.; Chen, R.; Song, Y.; Gao, J.; Sun, L.; Hou, J. Boosting Charge Mediation in Ferroelectric $BaTiO_{3-x}$-Based Photoanode for Efficient and Stable Photoelectrochemical Water Oxidation. *Small Struct.***2023**, *4*(9), 2300072. https://doi.org/10.1002/sstr.202300072.
170. Tymińska, N.; Wu, G.; Dupuis, M. Water Oxidation on Oxygen-Deficient Barium Titanate: A First-Principles Study. *J. Phys. Chem. C***2017**, *121*(15), 8378–8389. https://doi.org/10.1021/acs.jpcc.6b12425.
171. Fan, X. T.; Wen, X. J.; Zhuang, Y. B.; Cheng, J. Molecular insight into the GaP (110)-water interface using machine learning accelerated molecular dynamics. *J. Energy Chem.***2023**, *82*, 239–247.https://doi.org/10.1016/j.jechem.2023.03.013
172. Miao, L.; Jia, W.; Cao, X.; Jiao, L. Computational chemistry for water-splitting electrocatalysis. *Chem. Soc. Rev.***2024**, *53*(6), 2771–2807.https://doi.org/10.1039/D2CS01068B
173. Zhang, M.; Hou, Y. C.; Jiang, Y.; Ni, X.; Wang, Y.; Zou, X. Rational design of water splitting electrocatalysts through computational insights. *Chem. Commun.***2024**. https://doi.org/10.1039/D4CC05117C
174. Orhan, I.B.; Zhao, Y.; Babarao, R.; Thornton, A.W.; Le, T.C. Machine Learning Descriptors for CO_2 Capture Materials. *Molecules* **2025**, *30*, 650. https://doi.org/10.3390/molecules30030650
175. Ma, K.; Yang, C.; Zhang, J.; Li, Y.; Jiang, G.; Chai, J. Machine Learning-Assisted Hartree–Fock Approach for Energy Level Calculations in the Neutral Ytterbium Atom. *Entropy* **2024**, *26*, 962. https://doi.org/10.3390/e26110962
176. Tereshchenko, A.; Pashkov, D.; Guda, A.; Guda, S.; Rusalev, Y.; Soldatov, A. Adsorption Sites on Pd Nanoparticles Unraveled by Machine-Learning Potential with Adaptive Sampling. *Molecules* **2022**, *27*, 357. https://doi.org/10.3390/molecules27020357
177. Biswas, M.; Desai, R.; Mannodi-Kanakkithodi, A. Screening of novel halide perovskites for photocatalytic water splitting using multi-fidelity machine learning. *Phys. Chem. Chem. Phys.***2024**, *26*(35), 23177–23188.https://doi.org/10.1039/D4CP02330G

 doi:10.20944/preprints202506.0553.v1

178. Allam, O.; Maghsoodi, M.; Jang, S. S.; Snow, S. D. Unveiling competitive adsorption in TiO_2 photocatalysis through machine-learning-accelerated molecular dynamics, DFT, and experimental methods. *ACS Appl. Mater. Interfaces***2024**, *16*(28), 36215–36223.https://doi.org/10.1021/acsami.4c02334
179. Agrawal, S.; Wang, B.; Wu, Y.; Casanova, D.; Prezhdo, O. V. Photocatalytic activity of dual defect modified graphitic carbon nitride is robust to tautomerism: machine learning assisted ab initio quantum dynamics. *Nanoscale* **2024,** *16*(18), 8986–8995.https://doi.org/10.1039/D4NR00606B
180. Gao, Y.; Zhang, Q.; Hu, W.; Yang, J. First-principles computational screening of two-dimensional polar materials for photocatalytic water splitting. *ACS Nano***2024**, *18*(29), 19381–19390.https://doi.org/10.1021/acsnano.4c06544
181. Raman, A. S.; Vojvodic, A. Providing atomistic insights into the dissolution of rutile oxides in electrocatalytic water splitting. *J. Phys. Chem. C***2022**, *126*(2), 922–932.https://doi.org/10.1021/acs.jpcc.1c08737
182. Li, Z.; Wang, J.; Yang, C.; Liu, L.; Yang, J. Y. Thermal transport across TiO_2–H_2O interface involving water dissociation: Ab initio-assisted deep potential molecular dynamics. *J. Chem. Phys.***2023**, *159*(14).https://doi.org/10.1063/5.0167238
183. Jia, M.; Zhuang, Y. B.; Wang, F.; Zhang, C.; Cheng, J. Water-mediated proton hopping mechanisms at the SnO_2 (110)/H_2O interface from ab initio deep potential molecular dynamics. *Precis. Chem.***2024**, *2*(12), 644–654.https://doi.org/10.1021/prechem.4c00056
184. Schienbein, P.; Blumberger, J. Data-Efficient Active Learning for Thermodynamic Integration: Acidity Constants of $BiVO_4$ in Water. *ChemPhysChem* 2025, *26*(1), e202400490.https://doi.org/10.1002/cphc.202400490
185. Park, H.; Kim, Y.; Choi, S.; Kim, H. J. Data-driven computational design of stable oxygen evolution catalysts by DFT and machine learning: Promising electrocatalysts. *J. Energy Chem.***2024**, *91*, 645–655.https://doi.org/10.1016/j.jechem.2023.12.048
186. Wang, W.; Zhang, M.; Li, X.; Zhang, S.; Yu, F.; Li, S.; Comini, E.; Wang, Z. L.; Ren, K. Boosting efficiency in piezo-photocatalysis process using POLED $Ba_{0.7}Sr_{0.3}TiO_3$ nanorod arrays for pollutant degradation and hydrogen production. *ACS Appl. Mater. Interfaces***2024**. https://doi.org/10.1021/acsami.4c01287
187. Shao, Y.; de Ruiter, J.M.; de Groot, H.J.M.; Buda, F. Photocatalytic Water Splitting Cycle in a Dye-Catalyst Supramolecular Complex: Ab Initio Molecular Dynamics Simulations. *J. Phys. Chem. C* **2019**, *123*, 21403–21414.https://doi.org/10.1021/acs.jpcc.9b06401
188. Zhang, S.; Ye, H.; Hua, J.; Tian, H. Recent Advances in Dye-Sensitized Photoelectrochemical Cells for Water Splitting. *EnergyChem* **2019**, *1*, 100015.https://doi.org/10.1016/j.enchem.2019.100015
189. Nada, H.; Kobayashi, M.; Kakihana, M. Anisotropy in Conformation and Dynamics of a Glycolate Ion Near the Surface of a TiO_2 Rutile Crystal Between Its {001} and {110} Planes: A Molecular Dynamics Study. *J. Phys. Chem. C* **2016**, *120*, 6502–6514.https://doi.org/10.1021/acs.jpcc.5b11087
190. YazdanYar, A.; Aschauer, U.; Bowen, P. Interaction of Biologically Relevant Ions and Organic Molecules with Titanium Oxide (Rutile) Surfaces: A Review on Molecular Dynamics Studies. *Colloids Surf. B Biointerfaces* **2018**, *161*, 563–577.https://doi.org/10.1016/j.colsurfb.2017.11.004
191. Harmon, K.J.; Chen, Y.; Bylaska, E.J.; Catalano, J.G.; Bedzyk, M.J.; Weare, J.H.; Fenter, P. Insights on the Alumina–Water Interface Structure by Direct Comparison of Density Functional Simulations with X-ray Reflectivity. *J. Phys. Chem. C* **2018**, *122*, 26934–26944.https://doi.org/10.1021/acs.jpcc.8b08522
192. Biriukov, D.; Kroutil, O.; Předota, M. Modeling of Solid–Liquid Interfaces Using Scaled Charges: Rutile (110) Surfaces. *Phys. Chem. Chem. Phys.* **2018**, *20*, 23954–23966. https://doi.org/10.1039/C8CP04535F
193. Futera, Z.; English, N.J. Exploring Rutile (110) and Anatase (101) TiO_2 Water Interfaces by Reactive Force-Field Simulations. *J. Phys. Chem. C* **2017**, *121*, 6701–6711. https://doi.org/10.1021/acs.jpcc.6b12803
194. Cheng, J.; Sprik, M. Aligning Electronic Energy Levels at the TiO_2/H_2O Interface. *Phys. Rev. B* **2010**, *82*, 081406.https://doi.org/10.1103/PhysRevB.82.081406
195. Asproulis, N.; Drikakis, D. An Artificial Neural Network-Based Multiscale Method for Hybrid Atomistic-Continuum Simulations. *Microfluid Nanofluid* **2013**, *15*, 559–574. https://doi.org/10.1007/s10404-013-1154-4

 doi:10.20944/preprints202506.0553.v1

196. Smith, E.R.; Müller, E.A.; Craster, R.V.; Matar, O.K. A Langevin Model for Fluctuating Contact Angle BehaviourParametrised Using Molecular Dynamics. *Soft Matter* **2016**, *12*, 9604–9615. https://doi.org/10.1039/C6SM01980C
197. Smith, E.R.; Theodorakis, P.E.; Craster, R.V.; Matar, O.K. Moving Contact Lines: Linking Molecular Dynamics and Continuum-Scale Modeling. *Langmuir* **2018**, *34*, 12501–12518. https://doi.org/10.1021/acs.langmuir.8b00466
198. Zhang, X.; Bieberle-Hütter, A. Modeling and Simulations in Photoelectrochemical Water Oxidation: From Single Level to Multiscale Modeling. *ChemSusChem* **2016**, *9*, 1223–1242. https://doi.org/10.1002/cssc.201600214
199. Jung, C.K.; Braunwarth, L.; Jacob, T. Grand Canonical ReaxFF Molecular Dynamics Simulations for Catalytic Reactions. *J. Chem. Theory Comput.* **2019**, *15*, 5810–5816.https://doi.org/10.1021/acs.jctc.9b00687
200. Islam, M.M.; Kolesov, G.; Verstraelen, T.; Kaxiras, E.; van Duin, A.C.T. EReaxFF: A Pseudoclassical Treatment of Explicit Electrons within Reactive Force Field Simulations. *J. Chem. Theory Comput.* **2016**, *12*, 3463–3472.https://doi.org/10.1021/acs.jctc.6b00432
201. Tranca, D.C.; Zimmerman, P.M.; Gomes, J.; Lambrecht, D.; Keil, F.J.; Head-Gordon, M.; Bell, A.T. Hexane Cracking on ZSM-5 and Faujasite Zeolites: A QM/MM/QCT Study. *J. Phys. Chem. C* **2015**, *119*, 28836–28853.https://doi.org/10.1021/acs.jpcc.5b07457
202. Rusevich, L.L.; Kotomin, E.A.; Zvejnieks, G.; Popov, A.I. Ab initio calculations of structural, electronic and vibrational properties of $BaTiO_3$ and $SrTiO_3$ perovskite crystals with oxygen vacancies. *Low Temp. Phys.* **2020**, *46*, 1185–1195.
203. Eglitis, R.; Purans, J.; Popov, A.I.; Jia, R. Systematic trends in $YAlO_3$, $SrTiO_3$, $BaTiO_3$, $BaZrO_3$ (001) and (111) surface ab initio calculations. *Int. J. Mod. Phys. B* **2019**, 33, 1950390.
204. Eglitis, R.I.; Purans, J.; Popov, A.I.; Bocharov, D.; Chekhovska, A.; Jia, R. Ab initio computations of O and AO as well as ReO2, WO2 and BO2-terminated ReO3, WO3, BaTiO3, SrTiO3 and BaZrO3 (001) surfaces. *Symmetry* **2022**, 14, 1050.
205. Eglitis, R.I.; Kotomin, E.A.; Popov, A.I.; Kruchinin, S.P.; Jia, R. Comparative ab initio calculations of $SrTiO_3$, $BaTiO_3$, $PbTiO_3$ and $SrZrO_3$ (001) and (111) surfaces as well as oxygen vacancies. *Low. Temp. Phys.* **2022**, *48*, 80–88.
206. Eglitis, R.I.; Popov, A.I. Comparative ab initio calculations for ABO_3 perovskite (001), (011) and (111) surfaces as well as $YAlO_3$ (001) surfaces and *F* centers. *J. Nano Electron. Phys.* **2019**, *11*, 01001.